Threshold for Electron Trapping Nonlinearity in Langmuir Waves

D. J. Strozzi,[1, a] E. A. Williams,[1] H. A. Rose,[2] D. E. Hinkel,[1] A. B. Langdon,[1] and J. W. Banks[1]
[1] *Lawrence Livermore National Laboratory, Livermore, CA 94551, USA*
[2] *Los Alamos National Laboratory, Los Alamos, NM 87545, USA*

(Dated: 20 November 2012)

We assess when electron trapping nonlinearity is expected to be important in Langmuir waves. The basic criterion is that the inverse of the detrapping rate ν_d of electrons in the trapping region of velocity space must exceed the bounce period of deeply-trapped electrons, $\tau_B \equiv (n_e/\delta n)^{1/2} 2\pi/\omega_{pe}$. A unitless figure of merit, the "bounce number" $N_B \equiv 1/\nu_d\tau_B$, encapsulates this condition and defines a trapping threshold amplitude for which $N_B = 1$. The detrapping rate is found for convective loss (transverse and longitudinal) out of a spatially finite Langmuir wave. Simulations of driven waves with a finite transverse profile, using the 2D-2V Vlasov code LOKI, show trapping nonlinearity increases continuously with N_B for transverse loss, and significant for $N_B \approx 1$. The detrapping rate due to Coulomb collisions (both electron-electron and electron-ion) is also found, with pitch-angle scattering and parallel drag and diffusion treated in a unified manner. A simple way to combine convective and collisional detrapping is given. Application to underdense plasma conditions in inertial confinement fusion targets is presented. The results show that convective transverse loss is usually the most potent detrapping process in a single $f/8$ laser speckle. For typical plasma and laser conditions on the inner laser cones of the National Ignition Facility, local reflectivities $\sim 3\%$ are estimated to produce significant trapping effects.

PACS numbers: 52.25.Dg, 52.35.Fp, 52.35.Mw, 52.38.Bv, 52.38.-r, 52.57.-z
Keywords: nonlinear Langmuir waves; trapped electrons; laser-plasma interaction; inertial confinement fusion; stimulated Raman scattering

I. INTRODUCTION

The nonlinear behavior of Langmuir waves (LWs) is a much-studied problem in basic plasma physics from the 1950s to the present. In this paper, we focus on nonlinearity due to electron trapping in the LW potential well. This intrinsically kinetic effect has motivated theoretical work such as nonlinear equilibrium or Bernstein-Greene-Kruskal (BGK) modes[1], Landau damping reduction[2], nonlinear frequency shift[3–5], and the sideband instability[6,7]. Important applications of trapping occur in LWs driven by coherent (e.g., laser) light, including the laser plasma accelerator[8] and stimulated Raman scattering (SRS)[9–11]. The latter allows the prospect of laser pulse compression to ultra-high amplitudes (the backward Raman amplifier)[12]. In addition, SRS is an important risk to ICF[13,14], both due to loss of laser energy and the production of energetic (or "hot") electrons that can pre-heat the fuel. Ignition experiments at the National Ignition Facility (NIF)[15] have shown substantial Stimulated Raman backscatter (SRBS) from the inner cones of laser beams[16]. The current study is prompted primarily by SRS-driven LW's. Much recent work has focused on nonlinear kinetic aspects of SRS, including "inflation" due to Landau damping reduction[17–21], saturation by sideband instability[22], and LW self-focusing in multi-D particle-in-cell simulations[23–25], Vlasov simulations[26], and theory[27]. One goal is to find reduced descriptions, such as envelope equations, that approximately incorporate kinetic effects[28–30].

Our aim is to provide theoretical estimates for when electron trapping nonlinearity is important in LW dynamics. These allow for self-consistency checks - or invalidations - of linear calculations of LW amplitudes. This work is therefore not primarily intended to study nonlinear LW dynamics, although we do present Vlasov simulations to quantify the onset of trapping in the presence of convective transverse loss. We consider a single, quasi-monochromatic wave with electron number density fluctuation $\delta n(\vec{x}, t)\cos(kx - \omega t)$, and slowly-varying, unitless amplitude $\delta N \equiv \delta n/n_e$ where n_e is the background electron density. We refer to an electron as "trapped" if it is within the phase-space island centered about the phase velocity $v_p \equiv \omega/k$ and bounded by the separatrix in the instantaneous wave amplitude, regardless of how long it has been there. The dielectric response of the plasma depends on the distribution function, and therefore manifests trapping effects only after enough time has passed for the (typically space-averaged) distribution to be distorted. We call such a distribution trapped or flattened, since trapping produces a plateau in the space-averaged distribution centered at v_p. Deeply-trapped electrons have an angular frequency $\omega_B \equiv \omega_{pe}\delta N^{1/2}$ ($\omega_{pe}^2 = n_e e^2/\epsilon_0 m_e$ defines the plasma frequency in SI units), known as the bounce frequency, corresponding to a bounce period $\tau_B \equiv 2\pi/\omega_B \propto \delta N^{-1/2}$. In our language, an electron is trapped instantaneously, but a distribution becomes trapped over a time $\sim \tau_B$. For a process that detraps electrons at a rate ν_d, the unitless "bounce number" $N_B \equiv 1/\nu_d\tau_B$ measures how many

---

[a] Electronic mail: strozzi2@llnl.gov

bounce orbits a trapped electron completes before being detrapped.

Our estimates stem from the assumption that nonlinear trapping effects are significant when N_B is roughly unity. Trapping nonlinearity develops continuously with wave amplitude, and is not an instability with a hard threshold. Vlasov simulations presented in Sec. IV of driven LWs with a finite transverse profile demonstrate this. In addition, transit-time damping calculations[31] show the reduction in Landau damping varies continuously with N_B and obtains a 2x reduction for $N_B \approx 1$. Bounce number estimates are qualitative and demonstrate basic parameter scalings. The quantitative role of trapping depends on the specific application.

We consider two detrapping processes: convective loss and Coulomb collisions. For a LW of finite spatial extent, electrons enter and leave the wave from the surrounding plasma (assumed here to be in thermal equilibrium, i.e. Maxwellian). Trapping will only be effective if these electrons complete a bounce orbit before transiting the wave. We find the detrapping rate for both longitudinal end loss, which can be important in finite-domain 1D kinetic simulations, and for transverse side loss in 2D and 3D. To quantify the effect of trapping in a LW with finite transverse extent, we perform 2D-2V simulations with the parallel Vlasov code LOKI[26,32] of a LW driven by an external field with a smooth transverse profile. Our results are in qualitative agreement with Sec. IV of Ref. 26. That work considered a free LW excited by a driver of finite duration, while we consider a driver that remains on.

We present a unified calculation of collisional detrapping due to electron-ion and electron-electron collisions, including both pitch-angle scattering and parallel slowing down and diffusion. This relies on the fact that (see the Appendix) the distribution in the trapping region can be Fourier decomposed into modes $\sin[n\pi((v_x - v_p)/v_{tr} + 1/2)]$ for $n = 1, 3, ...$, and the diffusion rate of mode n is proportional to n^2. After a short time, only electrons in the fundamental $n = 1$ mode remain trapped. The collisional detrapping rate scales as $1/\delta N$, since the trapping width in velocity increases with wave amplitude. We discuss two ways to compare the relative importance of detrapping by side loss and collisions, which is complicated by their different scaling with δN.

Our calculations are applied to ICF plasma conditions, particularly LW's driven by stimulated Raman backscatter (SRBS) on the NIF. Transverse side loss out of laser speckles in a phase-plate-smoothed beam is generally a more effective detrapping process than collisions. The threshold δN for trapping to overcome side loss decreases with density and increases with temperature, while the collisional threshold decreases with density and slightly increases with temperature. For conditions typical of backscatter on NIF ignition experiments, namely T_e=2 keV and $n_e = 0.1n_{cr}$ with $n_{cr} \equiv \omega_0^2\epsilon_0 m_e/e^2$ the critical density for laser light of wavelength 351 nm, a reflectivity of $(5\times10^{13}\text{ W cm}^{-2}/I_0)^2$ produces linear Langmuir waves above the side loss threshold. Such values are likely to occur in intense speckles. We also show that smoothing by spectral dispersion (SSD)[33] is ineffective at detrapping in NIF-relevant conditions.

The paper is organized as follows. Section II provides some general considerations on our detrapping analysis. We present in Sec. III convective loss calculations for both longitudinal (end) and transverse (side) loss. Section IV contains Vlasov simulations with the LOKI code which study the competition of trapping and side loss. Detrapping by Coulomb collisions is treated in Sec. V. Our results are applied to SRBS in underdense ICF conditions in Sec. VI. We conclude in Sec. VII. The Appendix presents details of our collisional derivation and discusses the validity of our Fokker-Planck model.

II. GENERAL CONSIDERATIONS

This section presents our overall framework for estimating the trapping threshold, and lays out some definitions. Consider the trapped electrons in a LW field, attempting to undergo bounce orbits. There is a time-dependent condition for trapping to distort the distribution significantly, even in the absence of any detrapping process. For instance, if a LW is suddenly excited in a Maxwellian plasma, electrons execute bounce orbits according to what we call the dynamic bounce number

$$N_B^{\text{dyn}}(t) = \int_0^t \frac{dt'}{\tau_B(t')}. \tag{1}$$

The time dependence of τ_B allows for a slowly-varying wave amplitude $\delta n(t)$. Vlasov simulations presented in Sec. IV show that trapping starts to significantly affect the dielectric response when $N_B^{\text{dyn}} \approx 0.5$. That is, it takes a finite time for the distribution to reflect trapping. The early works of Morales and O'Neil[2,4] indicate such behavior, where the damping rate and frequency shift evolve over several bounce periods until approaching steady values as the system reaches a Bernstein-Greene-Kruskal (BGK) state[1].

To estimate the threshold for trapping to overcome a detrapping process, we assume the wave has been present long enough that $N_B^{\text{dyn}} \gtrsim 1$. The distribution has had enough time to become flattened, to the extent the detrapping process allows. For flattening to occur, an appreciable fraction of trapped electrons must remain so for about a bounce period before being detrapped. We are interested in the number of electrons in the trapping region, and how long they stay there.

We define the "trapping region" to extend from $u = u_p \pm u_{tr}/2$ where $u_{tr} \equiv 4(k\lambda_{De})^{-1}\delta N^{1/2}$ is the full width of the phase-space trapping island and $\lambda_{De} \equiv v_{Te}/\omega_{pe}$ with $v_{Te} \equiv (T_e/m_e)^{1/2}$. Throughout this paper, we use

$$u_X \equiv v_X/v_{Te} \tag{2}$$

to denote the scaled velocity v_X for various subscripts X. Let $N_{\text{tr}}(t)$ denote the fraction of electrons in the trapping region at the initial time $t = 0$, that continuously remain so to some later time t (note $N_{\rm tr}(t = 0) = 1$). At $t = 0$ we take the electron distribution to be Maxwellian. The fact that only some electrons in the trapping region lie within the separatrix (depending on their initial phase kx) is not relevant, since all the detrapping processes considered here are insensitive to the electron's phase in the wave. That is, the rate at which electrons leave the trapping region is independent of kx.

The detrapping rate ν_d is defined by assuming exponential decay for the trapped fraction: $N_{\rm tr} = e^{-\nu_d t}$. We allow for several independent detrapping processes to occur simultaneously, in that the overall detrapping rate $\nu_{d,O}$ is the sum of the rates $\nu_{d,i}$ for each ith process considered separately. Since a detrapping process generally does not strictly follow exponential decay, we choose a critical fraction $N^*_{\rm tr}$, which obtains for a critical time $t = t^*$, and let $\nu_d = \ln(1/N^*_{\rm tr})/t^*$. ν_d is independent of $N^*_{\rm tr}$ for exponential decay. We set $N^*_{\rm tr} = 1/2$ in what follows. Given the approximate nature of our calculation, further refinement of ν_d has little value.

In the literature, detrapping processes are sometimes approximated by a 1D kinetic equation with a Bhatnagar-Gross-Krook relaxation (or simply a Krook) operator[34]:

$$[\partial_t + v\partial_x - (e/m_e)E\partial_v]\, f = \nu_K \cdot (nf_0/n_0 - f). \qquad (3)$$

The linear electron susceptibility χ for this kinetic equation is

$$\chi(\omega, k) = -\frac{Z'(\zeta)}{2(k\lambda_{De})^2}\left[1 + i\frac{\nu_K}{kv_{Te}\sqrt{2}}Z(\zeta)\right]^{-1}, \qquad (4)$$

where $\zeta \equiv \omega/kv_{Te}\sqrt{2}$ and Z is the plasma dispersion function[35]. The Krook operator relaxes the electron distribution function f to an equilibrium f_0, and locally conserves number density $n = \int dv\, f$. The above operator does not conserve momentum or energy, although it can easily be generalized to do so. In a 1D-1V system, a Krook operator can mimic detrapping by transverse convective loss (a higher space-dimension effect) or Coulomb collisions (a higher velocity-dimension effect), such as in Ref. 36. Any perturbation from f_0 decays exponentially at the rate ν_K, so $\nu_d = \nu_K$ for such an operator. This is especially useful for a detrapping process which has ν_d independent of wave amplitude; this is the case for convective loss but not for collisions (as shown below). SRS simulations with a 1D Vlasov code and Krook operator, and its suppression of kinetic inflation, are presented in Ref. 37. In this paper, we do not use a Krook operator to model detrapping, although we do use one in our 2D Vlasov simulations to make them effectively finite in the transverse direction (a purely numerical purpose), and to include collisional LW damping in our application to ICF conditions in Sec. VI.

We take the bounce period of all trapped electrons to be τ_B, the result for deeply-trapped electrons. The actual period slowly increases to infinity for electrons near the separatrix. We then define the bounce number for process i as

$$N_{B,i} \equiv \frac{1}{\nu_{d,i}\tau_B} = \left[\frac{\delta N}{\delta N_i}\right]^{p_i}. \qquad (5)$$

We have expressed $N_{B,i}$ as a ratio of the LW amplitude to a "threshold" amplitude δN_i, to some power p_i. Recall that trapping effects like the Landau damping reduction develop continuously with δN, so the threshold for trapping nonlinearity is not a hard one. Besides the $\delta N^{-1/2}$ dependence of τ_B, $\nu_{d,i}$ also depends on δN in a process-dependent way. For $\nu_{d,i}$ independent of wave amplitude, which we show below is the case for convective loss, the power $p_i = 1/2$. This is not the case for detrapping by Coulomb collisions, which is shown in Sec. V to have $p_i = 3/2$. The overall detrapping rate $\nu_{d,O} = \sum_i \nu_{d,i}$, gives an overall bounce number via $N^{-1}_{B,O} = \sum_i N^{-1}_{B,i}$. We also define an overall threshold amplitude δN_O such that $N_{B,O}[\delta N = \delta N_O] = 1$; it is *not* generally true that $\delta N_O = \sum_i \delta N_i$.

III. CONVECTIVE LOSS: THEORY

In a LW of finite spatial extent, electrons remain in the trapping region only until they transit the wave. This detrapping manifests itself by longitudinal loss out of the ends of the wavepacket (the x direction for our field representation $\cos(kx - \omega t)$), as well as transverse loss out the sides. End loss is found by considering a wavepacket of length $L_{||}$ and infinite transverse extent. We work in the rest frame of the wavepacket, which may differ from the lab frame depending on application. For instance, a free LW propagates at group velocity $v_g = 3v^2_{Te}/v_p$ for $k\lambda_{De} \ll 1$, while a LW driven by a driver fixed in the lab frame (such as the ponderomotive drive in SRS) will essentially be at rest. For $v_{tr} \ll v_p$ we can treat all trapped electrons as moving forward at v_p. Thus for end loss $N_{\rm tr,el} = 1 - v_p t/L_{||}$. To find $\nu_{\rm d,el}$, we take $N^*_{\rm tr,el} = 1/2$, which gives $t^*_{\rm el} = L_{||}/v_p$ and $\nu_{\rm d,el} = K_{\rm el}v_p/L_{||}$ with $K_{\rm el} = \ln 2$. The bounce number for end loss is $N_{B,\rm el} = [\delta N/\delta N_{\rm el}]^{1/2}$, with exponent $p_{\rm el} = 1/2$ and threshold amplitude $\delta N_{\rm el} = [2\pi K_{\rm el}u_p\lambda_{De}/L_{||}]^2$. In practical units $\delta N_{\rm el} = (1.05 \times 10^{18}/n_{e,cc})T_{e,kV}(u_p/L_{||,\mu m})^2$ where $n_{e,cc}$ is in cm^{-3}, $T_{e,kV}$ is in keV, and $L_{||,\mu m}$ is in μm.

For transverse side loss, consider a cylindrical wavepacket of transverse diameter $L_\perp$ and infinite longitudinal length. In N total spatial dimensions, the cylinder has an $N - 1$ dimensional cross-section. Electrons with a Maxwellian distribution are transiting the cylinder, with unnormalized distribution $f_\perp = u_\perp^{N-2}\exp[-u_\perp^2/2]$ where $u_\perp$ is the transverse speed and $f_\perp du_\perp$ is the number of electrons per $du_\perp$. The average $u_\perp = ([\pi/2]^{1/2}, [8/\pi]^{1/2}) = (1.25, 1.60)$ for $N = (2, 3)$, indicating that detrapping is faster in 3D than in 2D.

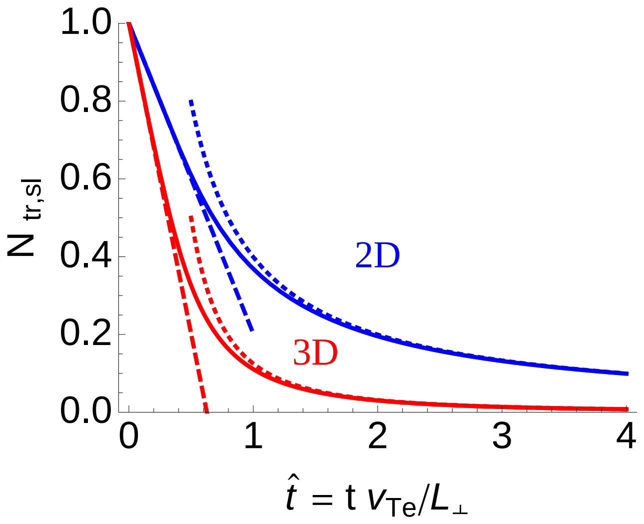

FIG. 1. (Color online.) Trapped electron fraction $N_{\mathrm{tr,sl}}$ due to transverse side loss for a 2D plane (blue) and 3D cylinder (red) region. The dashed curves are the appropriate early and late time limits. See Eqs. (6) through (12).

We find the number of initially trapped electrons ($|\vec{x}_\perp| < L_\perp/2$), that remain so after time t, by summing the fraction of electrons with a given $u_\perp$ that remain trapped, times $f_\perp$. All electrons with $|u_\perp| > 1/\hat{t}$ with $\hat{t} = tv_{Te}/L_\perp$ have escaped, so this sets the limits of integration. In 2D, the trapped fraction is $(1 - |u_\perp|\hat{t})$ for $|u_\perp| < 1/\hat{t}$, and the total trapped fraction is

$$N^{\mathrm{2D}}_{\mathrm{tr,sl}} = (2\pi)^{-1/2} \int_{-1/\hat{t}}^{1/\hat{t}} du_\perp\ e^{-u_\perp^2/2} \left[1 - |u_\perp|\hat{t}\right] \qquad (6)$$

$$= \mathrm{erf}\left[1/\hat{t}\sqrt{2}\right] + (2/\pi)^{1/2}\hat{t}(e^{-1/2\hat{t}^2} - 1). \qquad (7)$$

In 3D we obtain

$$N^{\mathrm{3D}}_{\mathrm{tr,sl}} = \int_0^{1/\hat{t}} du_\perp\ u_\perp\ e^{-u_\perp^2/2}\ \cdot \left[1 - \frac{2}{\pi}(\arcsin[u_\perp\hat{t}] + u_\perp\hat{t}[1-(u_\perp\hat{t})^2]^{1/2})\right]. \qquad (8)$$

The factor in square brackets is the trapped fraction. The limiting forms are

$$N^{\mathrm{2D}}_{\mathrm{tr,sl}}(\hat{t} \ll 1) \approx 1 - [2/\pi]^{1/2}\hat{t}, \qquad (9)$$

$$N^{\mathrm{2D}}_{\mathrm{tr,sl}}(\hat{t} \gg 1) \approx 1/[2\pi]^{1/2}\hat{t}, \qquad (10)$$

$$N^{\mathrm{3D}}_{\mathrm{tr,sl}}(\hat{t} \ll 1) \approx 1 - [8/\pi]^{1/2}\hat{t}, \qquad (11)$$

$$N^{\mathrm{3D}}_{\mathrm{tr,sl}}(\hat{t} \gg 1) \approx 1/8\hat{t}^2. \qquad (12)$$

In both limits the decrease is more rapid in 3D than in 2D. Figure 1 displays the various formulas for $N_{\mathrm{tr,sl}}(t)$.

The resulting detrapping rate, based on $N_{\mathrm{tr,sl}} = 1/2$, is

$$\nu_{\mathrm{d,sl}} = \frac{K_{\mathrm{sl}} v_{Te}}{L_\perp} \qquad (13)$$

with $K_{\mathrm{sl}} = (1.02, 2.08)$ in (2D, 3D). As expected, the 3D detrapping rate is faster. The 3D detrapping rate exceeds the 2D one by a larger factor than the average transverse speed because the faster electrons leave first, and the relative surplus of electrons in 3D over 2D (proportional to $u_\perp$) increases with transverse speed. A wavepacket with asymmetric (e.g. elliptical) cross-section should have a rate between the 2D and 3D result with $L_\perp$ taken as the shortest transverse length. In a laser beam smoothed with phase plates, elliptical speckles can be produced by certain polarization-smoothing schemes or a non-spherical lens; Langmuir waves driven by SRS in such speckles would also acquire an elliptical cross-section.

Comparing the end loss and side loss rates gives

$$\frac{\nu_{\mathrm{d,el}}}{\nu_{\mathrm{d,sl}}} = \frac{K_{\mathrm{el}}}{K_{\mathrm{sl}}} \frac{v_p}{v_{Te}} \frac{L_\perp}{L_{||}}. \qquad (14)$$

v_p is in the wavepacket frame. For the LW to not experience strong Landau damping, we have $v_p > v_{Te}$. $L_\perp/L_{||}$ depends on the physical situation (laser speckles are discussed in Sec. VI). The bounce number for side loss is analogous to end loss: $N_{B,\mathrm{sl}} = [\delta N/\delta N_{\mathrm{sl}}]^{1/2}$, with exponent $p_{\mathrm{sl}} = 1/2$ and threshold amplitude $\delta N_{\mathrm{sl}} = [2\pi K_{\mathrm{sl}}\lambda_{De}/L_\perp]^2$. In practical units and for the 3D K_{sl}, $\delta N_{\mathrm{sl}} = (9.44 \times 10^{18}/n_{e,cc}) T_{e,kV}/L^2_{\perp,\mu m}$.

IV. VLASOV SIMULATIONS OF CONVECTIVE SIDE LOSS

In this section, we quantify the competition between convective side loss and electron trapping in a driven Langmuir wave. We use the parallel, 2D-2V Eulerian Vlasov code LOKI[32]. This code employs a finite-volume method which discretely conserves particle number. The discretization uses a fourth-order accurate approximation for well-resolved features, and smoothly transitions to a third-order upwind method as the size of solution features approaches the grid scale. This construction enables accurate long-time integration by minimizing numerical dissipation, while retaining robustness for nonlinearly generated high frequencies. As a result, the method is not strictly monotone- or positivity-preserving, nor does it eliminate the so-called recurrence problem. This occurs at a recurrence time of $t_{rec} = \lambda/\Delta v$ when further linear evolution of a sinusoidal perturbation cannot be represented on a given grid.

Our simulations are 1D or 2D, with x the longitudinal coordinate as above, and y the transverse coordinate. Only electrons are mobile, there is a fixed, uniform neutralizing background charge, and there is no magnetic field. The total electric field is $\vec{E} = E_x\hat{x} + E_y\hat{y} = \vec{E}_d + \vec{E}_i$, where the internal electric field $\vec{E}_i = -\nabla\phi_i$ and $\nabla^2\phi_i = -\rho/\epsilon_0$. The external driver field is $\vec{E}_d = E_d\hat{x}$ with

$$E_d = E_0 A(t) h(y) \cos(k_0 x - \omega_0 t). \qquad (15)$$

There is no y component to the driver field, which would be needed if the driver were derived from a scalar potential. The temporal envelope $A(t)$ ramps up from zero to unity over a time $50/\omega_{pe}$ and then stays constant. The transverse profile $h(y)$ is

$$h(y) = \cos^2 \frac{2\pi y}{L_y} = \tfrac{1}{2}\left(1 + \cos k_1 y\right), \quad |y| < \frac{L_y}{4} \quad (16)$$

$$0 \quad \text{otherwise.} \quad (17)$$

$k_1 \equiv 4\pi/L_y$.

The numerical aspects of our runs are as follows. The x domain extends for one driver wavelength, with periodic boundaries for fields and particles. $N_x = 32$ zones in x was used for all runs in this paper, except for two $N_x = 64$ cases in Fig. 2(a). 2D runs had periodic boundaries for fields and particles at $|y| = L_y/2$. A Krook operator with $\nu_K(y) = 0$ for $|y| < 0.4L_y$ and rising rapidly in the boundary region $0.4 < |y|/L_y < 0.5$ was used to relax the distribution to the initial Maxwellian near the transverse boundaries. The runs were thus effectively finite in y. We used $N_y = 11$ to 45 zones in y, with more used for larger L_y and to check convergence. The v_x and v_y grids both extended to $\pm 7v_{Te}$. $N_{vy} = 32$ zones in v_y were used throughout. N_{vx} is set by two requirements: the trapping region must be adequately resolved, and recurrence phenomena must not be significant. We found $\Delta v_x \sim 0.1v_{tr}$ was sufficient to give converged results. LOKI's advection scheme is designed to mitigate aliasing problems, and we only saw modest effects related to it when comparing runs with different N_{vx}. The convergence of our numerical results is shown in Fig. 2(a). The black curve is typical: it uses $N_x = 32$ and has a typical $\Delta v_x/v_{tr}$, which we kept similar by varying N_{vx} with wave amplitude and k_0.

We first present 1D runs with $E_y = 0$ and $h(y) = 1$, which are detailed in Table I. From linear theory with $A(t) = 1$, $E_x = E_x^{\rm lin}\cos(k_0 x - \omega_0 t)$ where

$$\frac{E_x^{\rm lin}}{E_0} = \left|\frac{1}{1+\chi}\right| = \left[(1 + {\rm Re}\chi)^2 + ({\rm Im}\chi)^2\right]^{-1/2}. \quad (18)$$

χ is the linear electron susceptibility from Eq. (4) with $\nu_K = 0$, evaluated at the driver k_0 and ω_0. We chose ω_0 to give nearly the maximum $E_x^{\rm lin}$ for a given k_0. For $k_0\lambda_{De} < 0.53$, a linearly resonant ω_0 exists where $1 + {\rm Re}\chi = 0$; the maximum $E_x^{\rm lin}$ then occurs close to this point. No linear resonance exists for $k_0\lambda_{De} > 0.53$, which is called the loss of resonance[36]. Some ω_0 still maximizes $E_x^{\rm lin}$ in this regime. The non-resonant case differs from the resonant one, in that reducing ${\rm Im}\chi$ and Landau damping, e.g. by flattening the distribution at the phase velocity by electron trapping or some other means, does *not* lead to a large enhancement in the Langmuir wave response to an external drive. The term $1 + {\rm Re}\chi$ in Eq. (18) keeps $E_x^{\rm lin}$ finite even if ${\rm Im}\chi = 0$. For the parameters of the run `1D.7a`, we find $E_x^{\rm lin}/E_0 = 1.80$ for the full, complex χ, while setting ${\rm Im}\chi = 0$ slightly increases it to $E_x^{\rm lin}/E_0 = 2.01$.

TABLE I. 1D LOKI runs with no transverse driver profile $h(y)$. $\tilde{E}_0 = E_0 e/m_e v_{Te}\omega_{pe}$. $\tau_B^{\rm lin}$ is found using $E_x^{\rm lin}$.

Run	$k_0\lambda_{De}$	ω_0/ω_{pe}	$E_x^{\rm lin}/E_0$	$\tilde{E}_0$	$\tau_B^{\rm lin}\omega_{pe}$	plot curve
`1D.35a`	0.35	1.22	11.9	1.25×10^{-5}	871	red dash
`1D.35b`	”	”	”	5×10^{-5}	436	solid black
`1D.35c`	”	”	”	2×10^{-4}	218	blue dash
`1D.5a`	0.5	1.44	3.22	1.3×10^{-4}	434	black dash
`1D.5b`	”	”	”	5.2×10^{-4}	217	green dash
`1D.7a`	0.7	1.79	1.80	1.7×10^{-4}	430	black dot

Similar logic applies to kinetic inflation of stimulated Raman scattering. Electron trapping and the resultant Landau damping reduction can greatly increase the scattering at a resonant wavelength. However, scattering at a non-resonant wavelength is not subject to inflation, and can even decrease, due to reducing ${\rm Im}\chi$. Non-resonant SRS can occur in a situation seeded away from resonance[21], or if the plasma conditions are such that no resonance exists for any scattered wavelength, namely high T_e and low n_e.

Figure 2 presents the results of our 1D runs. Panel (a) shows the time evolution of the amplitude of E_x for $k = k_0$, normalized to the linear value from Eq. (18). Early in time ($\omega_{pe}t = 100 - 200$) the linear response is achieved, which validates the linear dispersion and properties of LOKI when using the chosen grid resolution. As time progresses the response increases due to the damping reduction, and then oscillates due to the interplay of the frequency shift and the fixed driver. Similar behavior was seen in Ref. 28. We plot the results vs. the dynamic bounce number $N_B^{\rm dyn}$ from Eq. (1), using the time-dependent E_x, in the center and right panels. $N_B^{\rm dyn}$ is thus a trapping-based re-scaling of time. The other runs from Table I are included as well. The driver strength E_0 was chosen in runs `1D.35b`, `1D.5a`, and `1D.7a` to give similar bounce periods. In all cases, the linear response is achieved after a transient period related to driver turn-on, until $N_B^{\rm dyn} \approx 0.5$. After this point the response increases, until the frequency shift develops at $N_B^{\rm dyn} \approx 1$. As $k_0\lambda_{De}$ increases, the enhancement above linear response decreases. This is likely due to the rapid increase of the frequency shift with $k\lambda_{De}$, as shown by most theoretical calculations, e.g. Ref. 4. For $k_0\lambda_{De} = 0.7$, there is a slight enhancement to 1.3x the linear response, followed by a dip to about 0.7x and subsequent oscillation about unity. This lack of significant trapping nonlinearity agrees with the above discussion of the non-resonant regime.

From Eq. (13), the 2D side loss rate is $\nu_{\rm d,sl} = 4.08v_{Te}/L_y$, where we have taken $L_\perp = L_y/4$, the full-width at half-max of $h(y)$. The side loss bounce number is then

$$N_{B,\rm sl} = \frac{L_y}{25.6\lambda_{De}}\delta N^{1/2}. \quad (19)$$

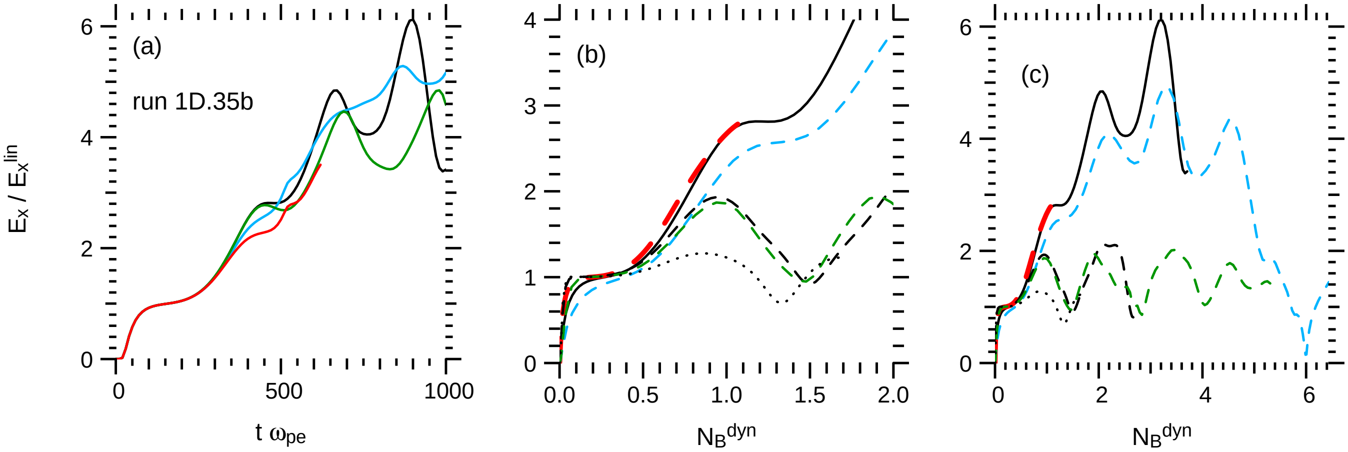

FIG. 2. (Color online.) (a) Amplitude of $k = k_0$ mode of E_x, scaled to linear response, vs. time for 1D LOKI case `1D.35b` and four different resolutions: $(N_x, N_{vx}) = (32, 768)$ (black), $(64, 768)$ (green), $(32, 384)$ (blue), and $(64, 384)$ (red). (b) E_x vs. dynamic bounce number $N_B^{\rm dyn}$ from Eq. (1) using $E_x(t)$ from 1D LOKI runs in Table I (see table for curve meanings). (c) panel (b) for expanded domain. The black curve is the only run in (a) that appears in (b) and (c).

TABLE II. 2D LOKI runs with transverse driver profile $h(y)$. All runs have $k_0\lambda_{De} = 0.35$, $\omega_0/\omega_{pe} = 1.22$, and $E_0 e/m_e v_{Te}\omega_{pe} = 2\times 10^{-4}$, the same as run `1D.35c`.

Run	L_y/λ_{De}	$N_{B,\rm sl} = L_y/884\lambda_{De}$	plot curve
`2D100`	100	0.113	red
`2D200`	200	0.226	dark blue
`2D400`	400	0.452	green
`2D800`	800	0.905	magenta
`2D1200`	1200	1.357	blue

Recall that electrons feel the total electric field $\vec{E}$ (drive plus interal), and δN is an equivalent density fluctuation. Gauss's law gives $\delta N = k_0\lambda_{De}\cdot\tilde{E}_x^0$, where E_x^0 is the amplitude of the k_0 Fourier mode of the on-axis field $E_x(y=0)$, and $\tilde{E} = Ee/m_e v_{Te}\omega_{pe}$ denotes a normalized field. Using the linear response from Eq. (18), we obtain the linear estimate

$$N_{B,\rm sl} = \frac{L_y}{25.6\lambda_{De}}\left|\frac{k_0\lambda_{De}}{1+\chi}\right|^{1/2}\tilde{E}_0^{1/2}. \qquad (20)$$

The 2D LOKI runs are listed in Table II. All runs used $k_0\lambda_{De} = 0.35$, $\omega/\omega_{pe} = 1.22$, and $\tilde{E}_0 = 2\times 10^{-4}$, the same as run `1D.35c`. For these values, our linear estimate becomes $N_{B,\rm sl} = L_y/884\lambda_{De}$.

The field magnitude $E_x(y=0)$ is plotted vs. the dynamic bounce number $N_B^{\rm dyn}$ found using E_x^0 for the 2D runs in Fig. 3. The black curve is the analogous 1D run `1D.35c`. For $N_B^{\rm dyn} \lesssim 4$ there is a continuous increase in the response with profile width L_y. This allows us to quantify trapping nonlinearity vs. L_y, which we do in Fig. 4. The abscissa in that figure is the side loss bounce number, $N_{B,\rm sl}$, computed with linear response as in Eq. (20). The ordinate is the field enhancement due to trapping, scaled to the same quantity for the 1D run. This is shown at times corresponding to several values of $N_B^{\rm dyn}$ ranging from 0.75 to 2. These times are early enough that the amplitudes have been mostly increasing, with little oscillation due to the frequency shift. The curves agree well, and demonstrate the continuous development of trapping effects with wide profiles. Slightly more than half the 1D trapping effect obtains for $N_{B,\rm sl} = 1$, which vindicates our $N_B \sim 1$ approximate threshold for trapping.

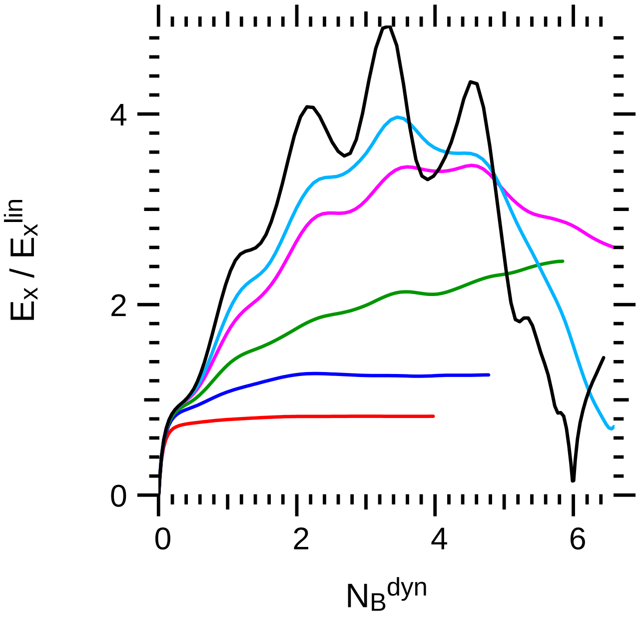

FIG. 3. (Color online.) Amplitude of $k = k_0$ mode of $E_x(y = 0)$ for 2D LOKI runs with transverse driver profiles $h(y)$ with various L_y. Run parameters and curve meanings are given in Table II. Black curve is 1D run `1D.35c`.

The plasma response to a driver with transverse pro-

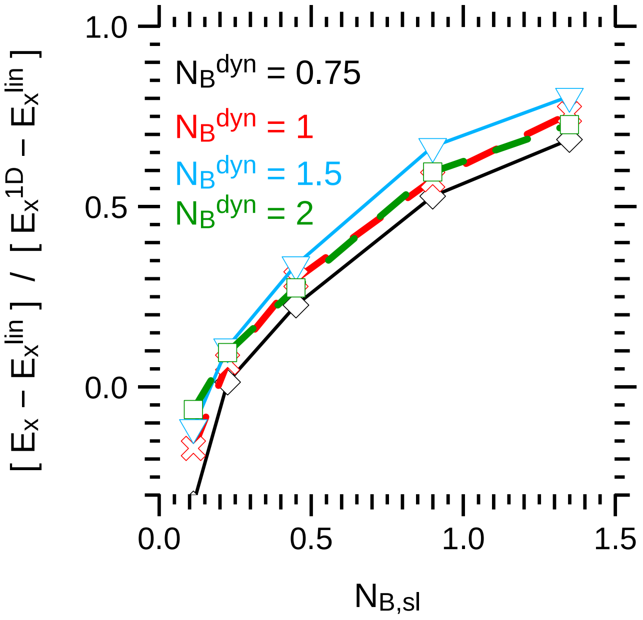

FIG. 4. (Color online.) Departure from linear response for 2D LOKI runs, scaled to the same quantity from the 1D run `1D.35c`. The colored curves are taken at times when the dynamic bounce number $N_B^{\rm dyn}$ has reached the value indicated by the colored text. $N_{B,\rm sl}$ is found from linear response, using Eq. (20).

file $h(y)$ differs from the 1D case. This can be seen in the ordinate of Fig. 4 falling below zero for the smallest $L_y = 100$. There have been several linear calculations of transit-time damping in LWs of finite extent, mostly by integration along particle orbits[38,39]. Ref. 38 showed that, for a potential with a step-function profile in space, the transit-time damping exceeds that for an infinite plane-wave for $\omega/kv_{Te} \gg 1$, while for $\omega/kv_{Te} \sim 1$ it can be less. We adopt the alternative approach of writing the response as a superposition of responses to the Fourier modes comprising the drive. This is particularly convenient for our $h(y)$, which (when periodically repeated) is composed of only two Fourier modes. For simplicity we present the result for $h(y)$ periodically repeated, instead of the actual LOKI profile with compact support over $|y| < L_y/4$. The compact case would lead to a continuous Fourier transform rather than discrete series, and introduce a line width around the dominant modes. This does not change the qualitative result. Unlike Ref. 38, our compact profile $h(y)$ is not a step function but smooth, with h and h' continuous at all points (although h'' is not).

The drive E_d, made periodic in y, is

$$E_d = \frac{E_0}{4} e^{i(k_0x-\omega_0t)} \left[1 + \frac{1}{2}e^{ik_1y} + \frac{1}{2}e^{-ik_1y}\right] + c.c. \quad (21)$$

A standard kinetic calculation, accounting for the fact that $\vec{E}_d$ has no y component and thus does not come from a potential, gives the field at $y = 0$:

$$E_x^{\rm lin}(x,t,y=0) = E_0|R|\cos(k_0x - \omega_0t + \alpha), \quad (22)$$

$$2R = \frac{1}{1+\chi_0} + \frac{1 + (1 + (k_0/k_1)^2)^{-1}\chi_+}{1+\chi_+}. \quad (23)$$

Note that the linear $E_y(y=0) = 0$ for our $\vec{E}_d$. α is a real phase. χ is the collisionless susceptibility for $\nu_K = 0$ from Eq. 4, which depends only on ω and $k = |\vec{k}|$. $\chi_0 = \chi(k_0,\omega_0)$ and $\chi_+ = \chi(k_+,\omega_0)$ with $k_+ = (k_0^2 + k_1^2)^{1/2}$. For $k_1 = 0$, we recover the 1D result Eq. (18). Physically, the higher-k modes induced by the transverse profile are more Landau damped (as well as being slightly off resonance for the fixed ω_0), which reduces the response. For the parameters of Table II, we find $|R|/|R|_{1D} = (0.801, 0.948)$ for $L_y = (100, 200)$ where $|R|_{1D} = 11.9$ is the value for $L_y \to \infty$. We obtain a slight decrease in the linear response for our sharpest profile ($L_y = 100$), and an insignificant change for wider ones. This is borne out by Fig. 3. The red curve for $L_y = 100$ shows no signs of trapping, and reaches a steady level slightly more than 0.8 times the 1D linear value. The blue curve ($L_y = 200$) shows a slight trapping enhancement, and reaches a steady level slightly above 1.2x linear after about 2 bounce periods.

V. COULOMB COLLISIONS

Collisions remove electrons from the trapping region via pitch-angle scattering (from electron-ion and electron-electron collisions) as well as parallel drag and diffusion (from only electron-electron collisions since $m_i/m_e \gg 1$). We adopt a Fokker-Planck collision operator, and discuss its validity in the Appendix:

$$\begin{aligned}\partial_t f = {} & \nu_0(1+Z_{\rm eff})u^{-3}\partial_\mu\left[(1-\mu^2)\partial_\mu f\right] \\ & + 2\nu_0 u^{-2}\partial_u(f + u^{-1}\partial_u f). \end{aligned} \quad (24)$$

$\mu = \cos\theta$ where θ is the pitch angle between $\vec{u}$ and the u_x direction, and $u = |\vec{u}|$. ν_0 is a thermal electron-electron collision rate:

$$\nu_0 \equiv \frac{\omega_{pe}\ln\Lambda_{ee}}{8\pi N_{De}}. \quad (25)$$

$N_{De} = n_e\lambda_{De}^3$ and $\ln\Lambda_{ee} = 24 - \ln(n_e^{1/2}/T_e)$ (n_e in cm^{-3}, T_e in eV) is the electron-electron Coulomb logarithm appropriate for $T_e > 10$ eV (Ref. 40, p. 34). The effective charge state is

$$Z_{\rm eff} \equiv \sum_i \frac{f_i Z_i^2}{\bar{Z}}\frac{\ln\Lambda_{ei}}{\ln\Lambda_{ee}}, \quad (26)$$

where $n_I = \sum_i n_i$ is the total ion density, $\bar{Z} = \sum_i Z_i f_i$ with $f_i = n_i/n_I$; $\sum_i f_i = 1$, and $\ln\Lambda_{ei}$ is the electron-ion Coulomb logarithm[40].

In section VI we apply our results to Langmuir waves generated by Raman scattering in underdense ICF plasmas, which are typically low-Z. For instance, NIF ignition hohlraum designs currently use an He gas fill (with H/He mixtures contemplated), and plastic ablators (57% H, 42% C atomic fractions). This gives $Z_{\rm eff}=5.08$ when fully-ionized and $\ln\Lambda_{ei}=\ln\Lambda_{ee}$. Be and diamond ablators are also being considered. For illustration, we take $Z_{\rm eff}=1$ as the lowest reasonable value (fully-ionized H), and use $Z_{\rm eff}=4$ (fully-ionized Be) to represent an ablator plasma.

It is useful to define a unitless time $\hat{t}$ (different from the side loss $\hat{t}$ used above), which demonstrates some of the basic collisional scaling:

$$\hat{t}\equiv\frac{\nu_c t}{\delta N}, \tag{27}$$

$$\nu_c\equiv\frac{\pi^2}{16}\frac{\nu_0}{u_p^3}(k\lambda_{De})^2=\frac{\pi}{128}\frac{(k\lambda_{De})^5}{(\omega/\omega_{pe})^3}\frac{\ln\Lambda_{ee}}{N_{De}}\omega_{pe}. \tag{28}$$

Our collisional calculation of the trapped fraction is detailed in the Appendix. The key observation is that the distribution in the trapping region can be decomposed into Fourier modes $\sin[n\pi((v_x-v_p)/v_{tr}+1/2)]$ for $n=1,3,...$, and the diffusion rate of mode n is proportional to n^2. After a short time, only electrons in the $n=1$ mode remain trapped, so it suffices to consider just the number in the $n=1$ mode. At $t=0$, this is 81% of the total (the other 19% rapidly diffuses out). The upshot is that $N_{\rm tr,c}$, the fraction of initially trapped particles remaining in the fundamental mode after time t, is

$$N_{\rm tr,c}(\hat{t},Z_{\rm eff},u_p)=0.81\int_0^\infty du_\perp u_\perp \exp\left[-u_\perp^2/2-D\hat{t}\right]. \tag{29}$$

$D(u_\perp,u_p,Z_{\rm eff})$ is given in Eq. (A12).

Eq. (29) is an implicit, integral equation for $\hat{t}$ as a function of $Z_{\rm eff}$, u_p, and $N_{\rm tr,c}$. We find the “exact” solution by performing the integral numerically, and interpolating $\hat{t}$ for a desired $N_{\rm tr,c}$. We derive an approximate solution, valid for $u_p\gg1$, for $\hat{t}$ in the Appendix. The result is

$$\hat{t}\approx\hat{t}_0+\hat{t}_1u_p^{-2}. \tag{30}$$

$\hat{t}_0$ and $\hat{t}_1$ are both positive and depend only on $Z_{\rm eff}$, so $\hat{t}$ decreases with increasing u_p. Figure 5 plots $N_{\rm tr,c}(\hat{t})$ for several u_p and $Z_{\rm eff}$, using the exact results (solid curves) and the approximate form for $u_p\to\infty$ of Eq. (A19) (dashed curves). Few electrons remain trapped at $\hat{t}=1$. The approximate forms are quite good, even though u_p is not that large.

Figure 6 displays the relative error $\epsilon\equiv1-\hat{t}_{\rm appr}/\hat{t}_{\rm ex}$ between $\hat{t}$ for $N_{\rm tr,c}=1/2$ computed two ways. The exact $\hat{t}_{\rm ex}$ is found numerically, and $\hat{t}_{\rm appr}$ is from Eq. (30), with Eq. (A20) for $\hat{t}_0$ and Eq. (A25) for $\hat{t}_1$. The agreement is excellent, within 1% for most of parameter space.

The collisional detrapping rate $\nu_{\rm d,c}$ is

$$\nu_{\rm d,c}=\frac{\nu_c}{\delta N}\frac{\ln(1/N_{\rm tr})}{\hat{t}}. \tag{31}$$

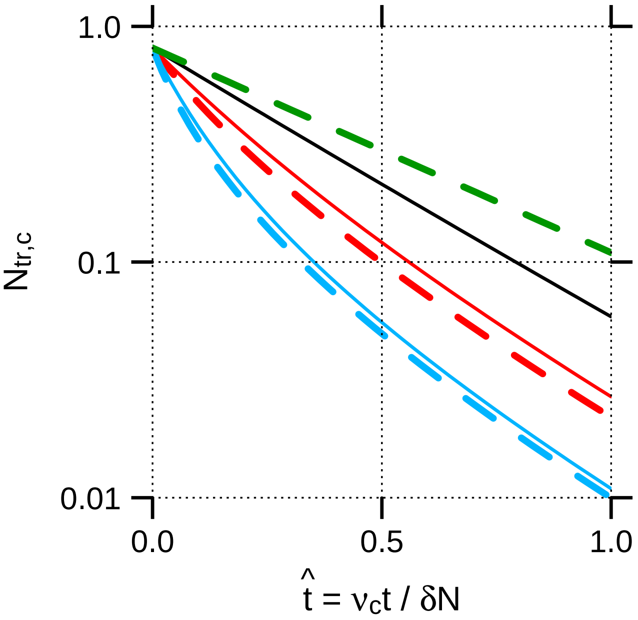

FIG. 5. (Color online.) Trapped fraction due to collisions $N_{\rm tr,c}$ vs. unitless time $\hat{t}$ defined in Eq. (27). Solid curves are exact results from Eq. (29). $(u_p,Z_{\rm eff})$ = (2,1), (4,1), and (4,4) for black, red, and blue, respectively. Dashed red and blue curves are approximate results for $u_p\to\infty$ from Eq. (A19), which depend only on $Z_{\rm eff}$ and not u_p. Green dashed curve is $0.81\exp[-2\hat{t}]$, the approximate form neglecting the term proportional to $\hat{t}$ in the denominator. $N_{\rm tr,c}(t=0)=0.81$ and not unity due to electrons not initially in the fundamental u_x mode.

Note that $\nu_{\rm d,c}\sim\delta N^{-1}$ since $u_{tr}\sim\delta N^{1/2}$: the larger the wave amplitude, the wider the trapping region extends in velocity, and collisions take longer to remove the electron velocity from this region. Recall that $\nu_{\rm d,c}$ depends slightly on the choice of $N_{\rm tr}$ due to the non-exponential decay of $N_{\rm tr}$ with $\hat{t}$; as with convective loss we choose $N_{\rm tr}=1/2$.

The collisional bounce number is

$$N_{B,c}=\left[\frac{\delta N}{\delta N_c}\right]^{3/2},\qquad \delta N_c=\left[2\pi\frac{\nu_c}{\omega_{pe}}\frac{\ln(1/N_{\rm tr})}{\hat{t}}\right]^{2/3}. \tag{32}$$

The amplitude exponent for collisions is $p_c=3/2$, unlike the convective loss value of 1/2. This stems from the fact that ν_d for collisions is amplitude-dependent while for convective loss it is not. We now construct the overall bounce number $N_{B,O}$ for convective side loss and collisions, as outlined above. Assuming that separate detrapping processes are independent, and their detrapping rates add, yields

$$N_{B,O}^{-1}=N_{B,\rm sl}^{-1}+N_{B,c}^{-1}=\left[\frac{\delta N_{\rm sl}}{\delta N}\right]^{1/2}+\left[\frac{\delta N_c}{\delta N}\right]^{3/2}. \tag{33}$$

We define an overall threshold amplitude δN_O such that $N_{B,O}[\delta N=\delta N_O]=1$. Eq. (33) gives a cubic equation

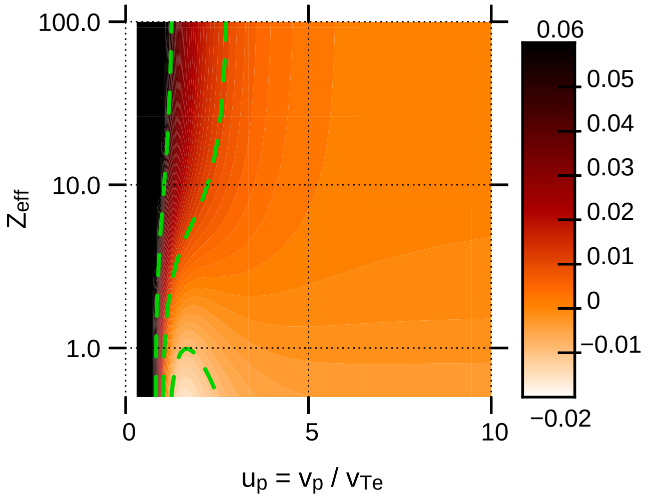

FIG. 6. (Color online.) Relative error $\epsilon = 1 - \hat{t}_{\rm appr}/\hat{t}_{\rm ex}$ between the exact and approximate results from Eqs. (29,30), respectively, for collisional $\hat{t}$; see text for details. The green curves are $\epsilon = [-0.01, 0.01, 0.05]$.

for $a \equiv \delta N_O^{1/2}$:

$$a^3 - \delta N_{\rm sl}^{1/2} a^2 - \delta N_c^{3/2} = 0. \tag{34}$$

There are two ways to compare the relative importance of side loss and collisions. One is: for which process must the wave amplitude δN be larger for trapping to be significant ($N_B = 1$)? The other is: for a given δN, which process will detrap more effectively? The two views are not equivalent, due to the different dependence of the side loss and collisional detrapping rate on δN. The first amounts to comparing the thresholds $\delta N_{\rm sl}$ and δN_c, which can be computed just from plasma and wave properties without knowing δN. The ratio of detrapping rates can be written in terms of a critical amplitude δN_{cr}:

$$\frac{\nu_{\rm d,c}}{\nu_{\rm d,sl}} = \frac{\delta N_{cr}}{\delta N}, \qquad \delta N_{cr} \equiv \frac{\ln 2}{\hat{t} K_{\rm sl}} \frac{\nu_c}{\omega_{pe}} \frac{L_\perp}{\lambda_{De}}. \tag{35}$$

VI. PARAMETER STUDY FOR ICF UNDERDENSE PLASMAS

We now apply our analysis to ICF conditions where stimulated Raman scattering (SRS) can occur, namely the underdense coronal plasma. SRS is a parametric three-wave process where a pump light wave such as a laser (we which label mode 0) decays to a scattered light wave (mode 1) and a Langmuir wave (mode 2). We restrict ourselves to exact backscatter (SRBS; $\vec{k}_1$ anti-parallel to $\vec{k}_0$), as this generates the largest k_2 (smallest v_{p2}/v_{Te}) and thus makes trapping effects more important (small transverse components to $\vec{k}_2$ have little effect on the phase velocity). Both measurements and simulations with the paraxial-envelope propagation code pF3D[41] have shown backscatter to be the dominant direction for SRS. With $\vec{k}_i = k_i\hat{z}$, the phase-matching conditions are $\omega_0 = \omega_1 + \omega_2$ and $k_0 = k_1 + k_2$ with $k_1 < 0$. We employ the (cold) light-wave dispersion relation $\omega_i^2 = (ck_i)^2 + \omega_{pe}^2$ for modes i =0 and 1, and use the vacuum wavelength $\lambda_i = 2\pi c/\omega_i$. Frequency matching thus requires $n_e < n_{cr}/4$, with $n_{cr,i} \equiv (\epsilon_0 m_e/e^2)\omega_i^2$ the critical density for mode i, and $n_{cr} = n_{cr,0}$. For specific examples we choose λ_0= 351 nm, appropriate for frequency-tripled UV light currently in use on NIF. Specific plasma conditions thought to be typical for SRBS on NIF ignition targets, during early to mid peak laser power, are $n_e/n_{cr} = 0.1$ and $T_e = 2$ keV ($\lambda_1 \approx 550$ nm)[42]. The scattered wavelength continuously increases during a NIF experiment, consistent with the hohlraum filling to higher density.

An important case for this paper is LW's driven by SRBS in the speckles of a phase-plate-smoothed laser beam[43]. For a laser wavelength λ_0 and square RPP with optics F-number F, the intense speckles have $L_\perp \approx F\lambda_0$ and $L_{||} \approx 5F^2\lambda_0$ (see Ref. 44). A speckled beam is not the only situation where SRS can occur; for instance, there has been recent interest in re-amplification of backscatter by crossing laser beams[45] and backward Raman amplifiers[46]. However, for a single laser beam, experiments at Omega and pF3D simulations show speckle physics, and its modification by beam smoothing, must be accounted for to accurately model SRS[47,48]. Experiments have also verified the increase in backscatter with increased gain per speckle length, by changing the laser aperture and thus the effective F[49]. We therefore focus on speckles. On NIF, four laser beams, each smoothed by a phase plate and with an overall $F = 22$ square aperture, are grouped into a "quad" which yields an effective square aperture of $F \approx 8$. We thus use $F = 8$ for illustration. As the beams of a quad propagate through a target, they can separate from one another, refract, and undergo other effects that change the shape of their effective aperture and speckle pattern. We do not pursue this further here, but it should be born in mind when applying our analysis. Also the ratio $L_\perp/L_{||} = 1/5F$ is so small that $\nu_{\rm d,el}/\nu_{\rm d,sl} \approx (K_{\rm el}/K_{\rm sl})u_p/5F = 0.0083u_p$ (3D) is small for essentially all speckles of interest. Thus side loss is a more potent detrapping mechanism than end loss, in speckles.

To quantify detrapping rates, we consider the threshold amplitudes $\delta N_{\rm sl}$ and δN_c. Unlike $\delta N_{\rm sl}$, δN_c depends on ω_2 and k_2 of the Langmuir wave. For a given set of plasma conditions, the choice of (ω_2, k_2) is not unique but depends on the application. For SRS developing locally, one can choose the LW corresponding to the largest growth rate for those conditions. Another approach is to consider a single scattered-light frequency as it propagates through a target. We consider only k variations induced by spatial profiles and not ω variations due to temporal plasma evolution[50] (which is mostly relevant to stimulated Brillouin scattering). In this case, the matching conditions given the local plasma properties dictate

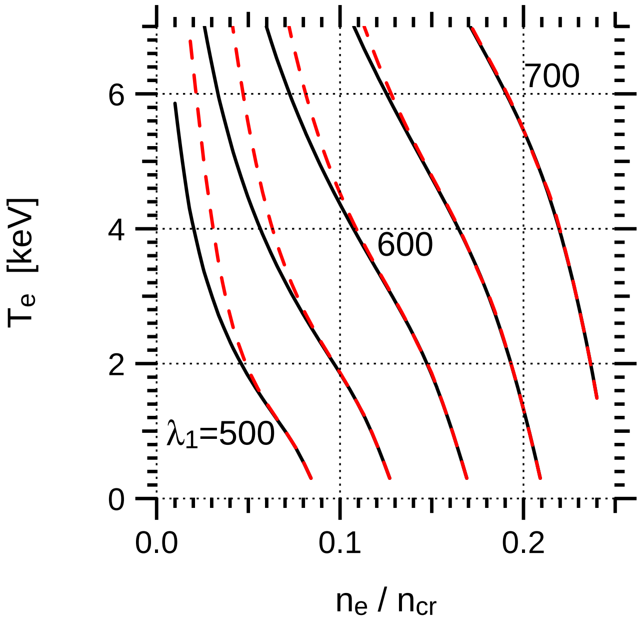

FIG. 7. (Color online.) Wavelength λ_1 in nm for SRBS light (increments of 50 nm), for a pump wavelength λ_0= 351 nm. Black solid: λ_1 phase-matched with a natural Langmuir wave, satisfying the dispersion relation Eq. (36) with $\nu_K = 0$. Red dash: λ_1 for the maximum local SRBS spatial gain rate.

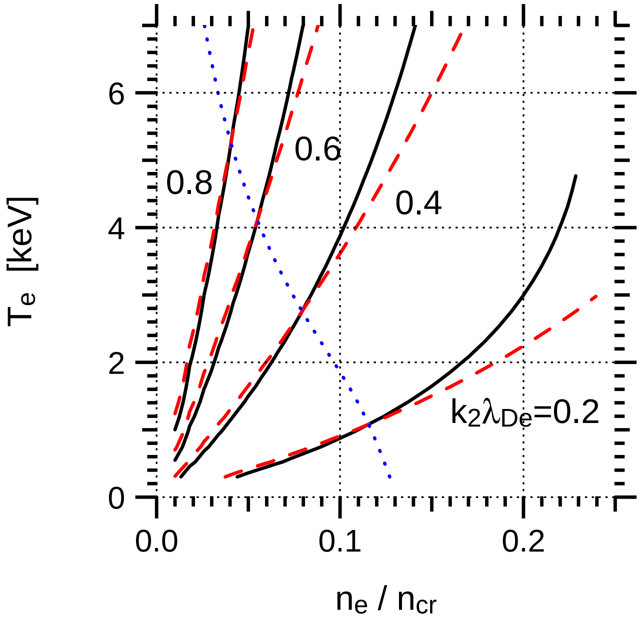

FIG. 8. (Color online.) Langmuir wave $k_2\lambda_{De}$ phase-matched for SRBS with different λ_1 choices, for a pump wavelength λ_0= 351 nm. Black solid: λ_1 phase-matched with a natural Langmuir wave, as in black solid curves of Fig. 7. Red dash: λ_1=550 nm (ω's fixed, k's vary). Blue dot: λ_1=550 nm black-solid contour from Fig. 7.

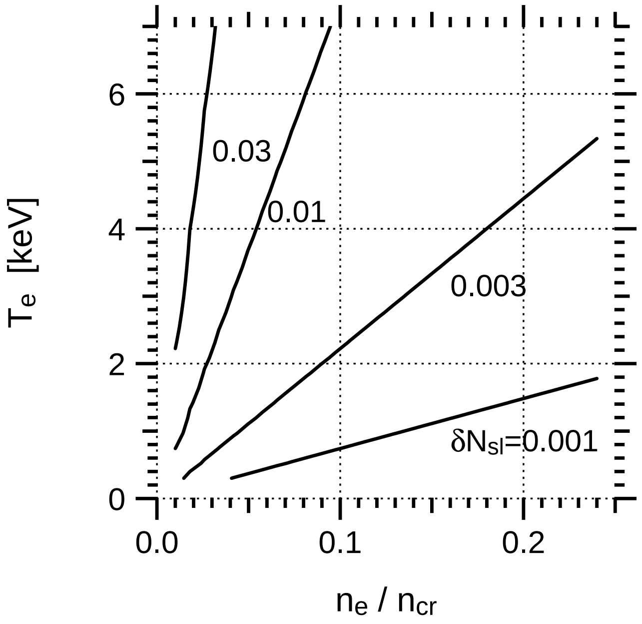

FIG. 9. Threshold Langmuir wave amplitude for side loss, δN_{sl}, for $L_\perp$=8×351 nm.

how k_2 varies.

Figure 7 presents the local λ_1 for SRBS computed in two ways. The black curves are found by phase-matching with a "natural" LW, by which we mean $\omega_2 = \mathrm{Re}[\omega_{2c}]$ where complex ω_{2c} satisfies

$$1 + \chi[k_{2r}, \omega_{2c}] = 0 \tag{36}$$

with real $k_{2r} = k_0 - k_1$. To find ω_{2c}, we set $\nu_K = 0$ and recover the usual collisionless χ. We use $\nu_K \neq 0$ below as a simple way to include collisional LW damping when Landau damping is negligible. The red curves in Fig. 7 are the λ_1 which maximizes the local spatial SRBS gain rate in the strong damping limit[51]:

$$\partial_z \ln i_1(\lambda_1, z) = \left[-\frac{2\pi r_e}{m_e c^2}\frac{I_0}{\omega_0 k_0}\right]\left[\frac{k_2^2}{|k_1|}\mathrm{Im}\frac{\chi}{1+\chi}\right]. \tag{37}$$

We use the collisionless χ with $\nu_K = 0$. The first bracket is independent of λ_1, while the second bracket is not. The two results for λ_1 in Fig. 7 are very close except for high-$k_2\lambda_{De}$ LW's (low n_e, high T_e), where Landau damping and its variation with λ_1 is significant. We choose for convenience to use λ_1 matched to a natural LW below. We display in Fig. 8 the $k_2\lambda_{De}$ corresponding to two choices of λ_1. The black curves use the λ_1 phase-matched to a natural LW (the black curves in Fig. 7), while the red curves are for a constant λ_1= 550 nm.

The side loss threshold δN_{sl} is shown in Fig. 9, for $L_\perp = F\lambda_0$ and $F = 8$. It simply represents the variation in λ_{De}, and is independent of (ω_2, k_2). Figure 10 depicts the collisional threshold δN_c for Z_{eff}= 1 and 4. The decrease of δN_c with electron density is mainly due to the decrease of the $(k\lambda_{De})^5$ factor in ν_c (see Eq. (28)),

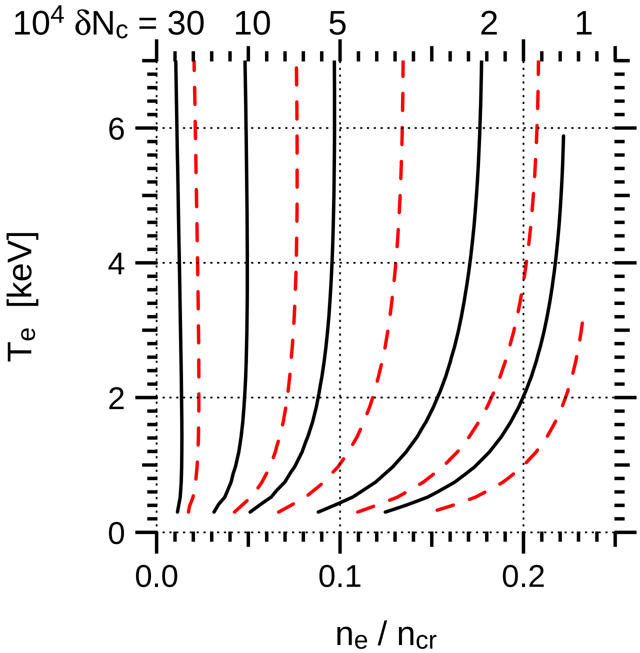

FIG. 10. (Color online.) Threshold Langmuir wave amplitude for collisions, δN_c. LW ω_2 and k_2 are for phase-matched SRBS with a natural LW (black solid curves of Fig. 7), and pump wavelength λ_0= 351 nm. Black solid: $Z_{\rm eff}$=1. Red dash: $Z_{\rm eff}$=4. From right to left, curves are for $\delta N_c = [1, 2, 5, 10, 30] \times 10^{-4}$.

which in turn is due to the $1/v_p^3$ fall in the Coulomb cross-section (see Eq. (25)). The ratio $\delta N_c/\delta N_{sl}$ is displayed in Fig. 11, which indicates collisions have a minor effect except for low n_e and low T_e; this relative importance depends strongly on the transverse length $L_\perp$ chosen for side loss. Figure 12 plots the critical amplitude δN_{cr} from Eq. (35). For $\delta N > \delta N_{cr}$, the side loss detrapping rate exceeds the collisional rate. δN_{cr} is larger at smaller n_e, indicating collisional detrapping is more relevant. 2D particle-in-cell simulations with the VPIC code of Raman amplifier experiments[45,52] found that collisions mattered for low-intensity seed light waves in a low-density plasma ($n_e/n_{cr} \sim 0.01$).

The reflectivities which correspond to trapping nonlinearity can also be estimated. We assume the LW's are in the strong damping limit[51], and write

$$\delta N = \frac{1}{2}\frac{(k_2\lambda_{De})^2}{|1+\chi|}\frac{V_0 V_1}{v_{Te}^2}. \tag{38}$$

$V_i = eE_i/m_e\omega_i$ is the oscillation velocity for light wave i; in practical quantities we have $(V_i/c)^2 = I_i\lambda_i^2/\eta_i P_0$, with $P_0 \equiv 2\pi^2(\epsilon_0/e^2)m_e^2c^5 = 1.37\times10^{18}$ W cm$^{-2}\cdot\mu$m^2. $\eta_i = [1 - n_e/n_{cr,i}]^{1/2}$ reflects the decrease in group velocity. With reflectivity $R = I_1/I_0$, we find

$$\delta N = \frac{I_0}{I_{cr}}R^{1/2}, \tag{39}$$

$$I_{cr} \equiv 2\frac{|1+\chi|}{(k_2\lambda_{De})^2}\frac{T_e}{m_ec^2}\frac{P_0}{\lambda_0\lambda_1}(\eta_0\eta_1)^{-1/2}. \tag{40}$$

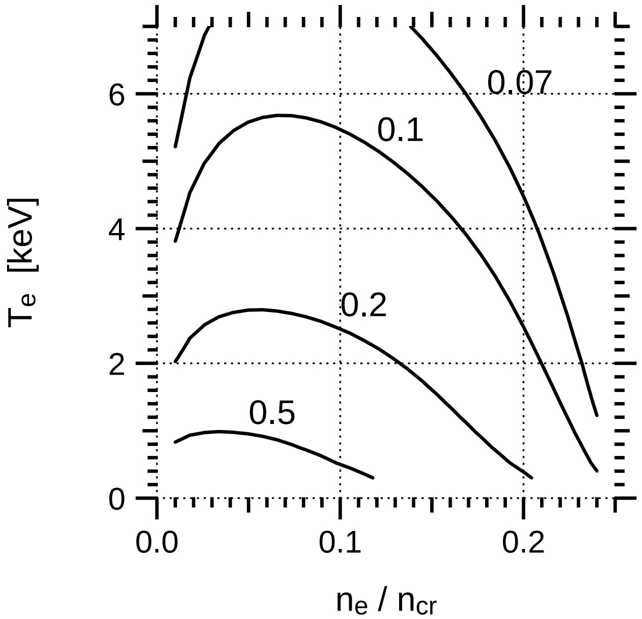

FIG. 11. Ratio $\delta N_c/\delta N_{\rm sl}$ from Figs. 9 and 10 for $Z_{\rm eff}$=4.

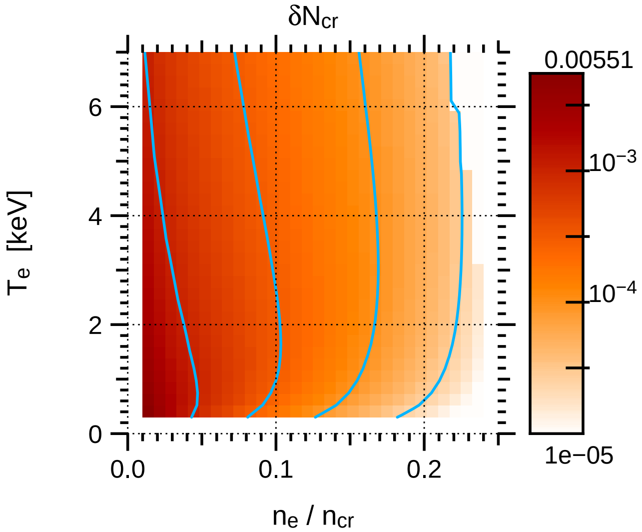

FIG. 12. (Color online.) Critical amplitude δN_{cr} from Eq. (35) for $Z_{\rm eff}$=4. The side loss detrapping rate is faster than the collisional one for $\delta N > \delta N_{cr}$. Blue curves are for $\delta N_{cr} = 3\times10^{-5}, 1\times10^{-4}, 3\times10^{-4}, 1\times10^{-3}$.

The "critical intensity" I_{cr} is introduced for convenience. Since trapping effects become significant for $\delta N \approx \delta N_i$ where δN_i is the detrapping threshold for process i, we define the threshold reflectivity $R_{\rm thr,i}$ for which $\delta N = \delta N_i$:

$$R_{\rm thr,i} = \left[\frac{I_{cr}}{I_0}\delta N_i\right]^2. \tag{41}$$

To illustrate the threshold reflectivity, we consider SRBS of the phase-matched natural LW. The critical intensity I_{cr} is plotted in Fig. 13. We use χ from Eq. (4)

including the Krook operator $\nu_K \neq 0$ to damp the LW when $k_2\lambda_{De}$ is small and Landau damping is ineffective. For this purpose we choose ν_K to be the collisional, unmagnetized frictional drag rate in the electron momentum equation[53,54]. This rate is appropriate for the drag on the bulk sloshing motion of the electrons in the LW electric field, and not collisions of resonant electrons with $v \approx v_p$. I_{cr} minimizes near the lower-right corner near the 2.5×10^{14} curve, where Landau and collisional damping are both weak. The threshold reflectivity $R_{\mathrm{thr,sl}}$ to overcome side loss is plotted in Fig. 14, for a pump with $I_0 = 10^{15}$ W/cm^2. A small reflectivity produces a large LW in the lower-right corner where damping is weak, thus allowing trapping to more easily occur.

Our analysis assumes a Maxwellian electron distribution f. This is not well known in ICF plasmas, and is an active area of research. For instance, nonlocal transport due to scale lengths that are not sufficiently short compared to collisional mean free paths, as well as hot electron generation by SRS-produced LWs, lead to significant non-Maxwellian features. This becomes more important for speeds larger than the thermal speed, where collisions become less effective and which LW phase velocities generically are. The dominant effect of non-thermal f on our analysis is via the collisionless part of Imχ and the LW Landau damping rate, which depends sensitively on $f(v_p)$, while Reχ and the real frequency are determined by the bulk motion of the entire f. The low T_e, high n_e parameter region, with small $k\lambda_{De}$ and large v_p/v_{Te}, is where the Landau damping is most susceptible to non-thermal f. But the Landau damping is quite small here for a Maxwellian, and is dominated by collisional damping. The latter relies on the scattering of the bulk electrons on ions, and is therefore not very sensitive to details of f. Our results should be somewhat insensitive to the presence of non-Maxwellian tails.

We now consider the specific plasma conditions mentioned above as typical for SRBS on NIF ignition experiments, namely $n_e/n_{cr} = 0.1$ and $T_e = 2$ keV[42]. The phase-matched SRBS modes have $\lambda_1 = 553$ nm, $k_2\lambda_{De} = 0.297$, and $\omega_2/\omega_{pe} = 1.155$. The calculated backscatter gain rate is significant in both the CH ablator and He gas fill. The material affects a trapping assessment only via collisions. From Fig. 11, for $Z_{\mathrm{eff}} = 4$ we find $\delta N_c/\delta N_{sl} = 0.24$, so we just consider side loss. The 3D side loss detrapping rate is $\nu_{\mathrm{d,sl}} = 13.9$/ps, or a time of $1/\nu_{\mathrm{d,sl}} = 0.072$ ps. The side loss threshold is $\delta N_{\mathrm{sl}} = 2.7 \times 10^{-3}$, the critical intensity is $I_{cr} = 1.96 \times 10^{16}$ W/cm^2, and the threshold reflectivity is $R_{\mathrm{thr,sl}} = (5.28 \times 10^{13}\ \mathrm{W\ cm^{-2}}/I_0)^2$. A typical intensity for inner cones of lasers in NIF ignition experiments of $I_0 = 3 \times 10^{14}$ W/cm^2 gives $R_{\mathrm{thr,sl}} = 0.03$. Larger beam-averaged reflectivities are frequently measured in experiments, and even larger values will occur in intense speckles.

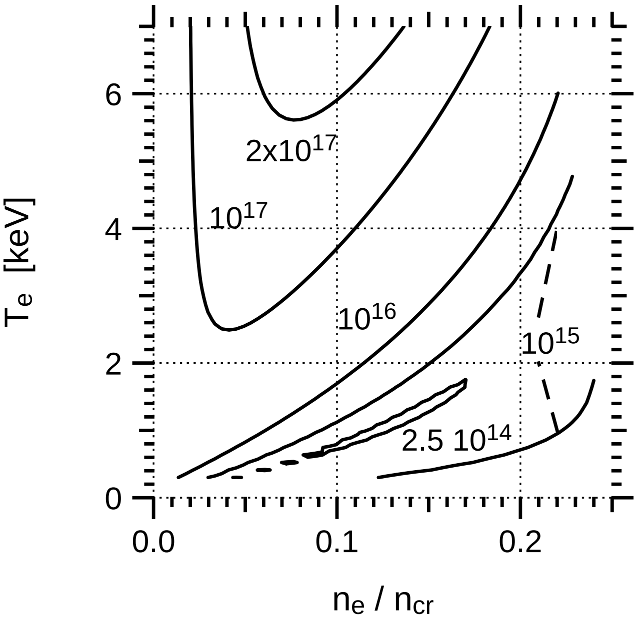

FIG. 13. Critical intensity I_{cr} from Eq. (40) in W/cm^2 relating laser intensity I_0 and reflectivity R to LW amplitude: $\delta N = (I_0/I_{cr})R^{1/2}$.

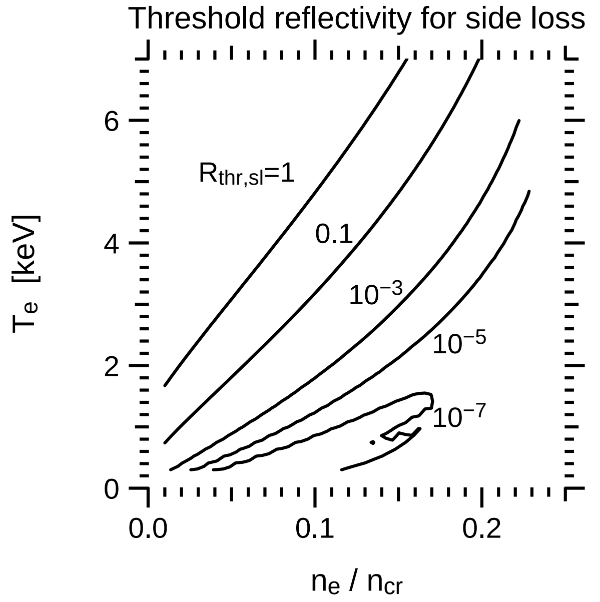

FIG. 14. Threshold reflectivity $R_{\mathrm{thr,sl}} \propto 1/I_0^2$ from Eq. (41) to overcome side loss for $I_0 = 10^{15}$ W/cm^2.

Finally, we show that smoothing by spectral dispersion (SSD)[33] is not likely to reduce trapping effects in SRBS on NIF. Recent experiments have utilized $\Delta f_1 = 45$ GHz of SSD bandwidth in the fundamental, 1054 nm laser light. After frequency-tripling, this corresponds to a speckle lifetime of $t_{ssd} = 1/(3\Delta f_1) = 7.4$ ps. For the reference SRBS conditions discussed above, $t_{ssd} \sim 100/\nu_{\mathrm{d,sl}}$. Thus SSD is much less effective at detrapping than side loss. Moreover, a Langmuir wave overcomes SSD detrapping ($\tau_B < t_{ssd}$) for a very low amplitude of $\delta N = 2.5 \times 10^{-7}$, or a reflectivity of $(4.9 \times 10^9\ \mathrm{W\ cm^{-2}}/I_0)^2$.

VII. CONCLUSIONS AND FUTURE PROSPECTS

This paper presented a framework for estimating when electron trapping nonlinearity becomes important in Langmuir-wave dynamics. Detrapping by convective loss in the longitudinal and transverse directions were discussed, as well as detrapping by Coulomb collisions (electron-electron and electron-ion). 2D-2V simulations with the Vlasov code LOKI quantified trapping effects in driven LWs with finite transverse profiles, and showed they increase with the side loss bounce number as the transverse width increases. These runs showed trapping has little importance for $k\lambda_{De} = 0.7$, which is above the loss of resonance value of 0.53. We explained this in terms of Eq. (18), and related it to the lack of kinetic inflation in non-resonant Raman scattering.

We applied our results to LWs driven by SRBS in NIF-relevant conditions. An $f/8$ intense laser speckle was taken as the LW size in order to estimate side loss. Side loss from speckles is generally more effective at detrapping electrons than collisions, although this is not the case for wider LWs or high-Z plasmas. Linear response at the locally resonant SRBS scattered wavelength allowed us to obtain an local reflectivity needed for trapping to overcome side loss. This gives small values ($\sim 1\%$) for plasma conditions from which SRBS is thought to originate in current NIF experiments. Moreover, it is the speckle, and not the lower beam average, intensity that matters. Preliminary assessment of pF3D simulations[55] of NIF targets indicates a significant fraction of SRBS-generated LWs is above our trapping threshold. Future work will assess this, and attempt to incorporate trapping effects into enveloped propagation codes like pF3D.

ACKNOWLEDGMENTS

We gratefully recognize J. A. F. Hittinger and R. L. Berger for helpful discussions and support. Work at LLNL was supported by US Dept. of Energy Contract DE-AC52-07NA27344 and partly under LDRD tracking number 12-ERD-061.

Appendix A: Derivation of collisional results

We restate our collision operator from Eq. (24):

$$\frac{1}{\nu_0}\frac{\partial f}{\partial t} = (1+Z_{\mathrm{eff}})u^{-3}\partial_\mu\left[(1-\mu^2)\partial_\mu f\right] + 2u^{-2}\partial_u(f+u^{-1}\partial_u f). \tag{A1}$$

The second term describes collisions of tail electrons off bulk electrons, and is valid for $u_p \gg 1$. The parallel (u_x) and perpendicular ($u_\perp$) velocities are given by $u_x = \mu u$ and $u_\perp = [1-\mu^2]^{1/2}u$ with $u \in [0,\infty]$ and $\mu \in [-1,1]$. We compute N_{tr}, the number of electrons initially trapped, that remain so up to time t. That is, once an electron leaves the trapping region its coherent bounce motion stops, even if it re-enters the trapping region later. The trapping region extends from $u_x = u_p \pm u_{tr}/2$ and over all $u_\perp$.

Changing variables from (μ, u) to $(u_\perp, u_x)$ gives

$$\frac{1}{\nu_0}\frac{\partial f}{\partial t} = \big[D_{xx}\partial^2_{u_x^2} + D_x\partial_{u_x} + D_{x\perp}\partial^2_{u_x u_\perp} + D_\perp\partial_{u_\perp} + D_{\perp\perp}\partial^2_{u_\perp^2}\big]f. \tag{A2}$$

The D's are straightforward to work out, and we do not give them. We assume u_{tr} is small, and order derivatives as $\partial/\partial u_x \sim 1/u_{tr}$ and $\partial/\partial u_\perp \sim 1$ ($v_\perp \sim v_{Te}$ in physical units). For sufficiently small u_{tr}, the dominant term is $D_{xx}\partial^2 f/\partial u_x^2$. For $u_p \gg 1$, this is valid if $u_{tr} \ll F(Z_{\mathrm{eff}})/u_p$ where F is a function of Z_{eff}. With this approximation, the collision operator yields a 1D diffusion equation:

$$\frac{1}{\nu_0}\frac{\partial f}{\partial t} = D_{xx}\frac{\partial^2 f}{\partial u_x^2}, \tag{A3}$$

$$D_{xx} \equiv \frac{(u_\perp^2+u_p^2)u_\perp^2(1+Z_{\mathrm{eff}})+2u_p^2}{(u_\perp^2+u_p^2)^{5/2}}. \tag{A4}$$

We solve this equation subject to the outflow boundary conditions $f(u_x = u_\pm, u_\perp, t) = 0$ with $u_\pm = u_p \pm u_{tr}/2$ the boundaries of the trapping region. The initial condition for the trapped distribution is $f = f_0\exp[-(u_\perp^2 + u_p^2)/2]$ (a Maxwellian with u_x evaluated at u_p) inside the trapping region, and $f = 0$ otherwise. The number of trapped electrons is

$$N_{\mathrm{tr}} = 2\pi\int_0^\infty du_\perp\, u_\perp \int_{u_-}^{u_+} du_x f. \tag{A5}$$

We choose $f_0 = (2\pi u_{tr})^{-1}e^{u_p^2/2}$ so $N_{tr}(t=0) = 1$. f has the solution

$$f = \sum_{n=1,3,\ldots} f_n(u_\perp, t)\sin n\pi w, \tag{A6}$$

$$f_n = \frac{2}{\pi^2 n u_{tr}}\exp[-u_\perp^2/2 - n^2 D\hat{t}]. \tag{A7}$$

$w \equiv (u_x - u_-)/u_{tr}$, $\hat{t}$ is given by Eq. (27), and $D \equiv D_{xx}u_p^{-3}$. The sum is over odd positive integers since the even terms vanish. The trapped fraction becomes

$$N_{\mathrm{tr}} = \frac{8}{\pi^2}\sum_n n^{-2}\int_0^\infty dx\exp[-x - n^2 D\hat{t}]. \tag{A8}$$

$x \equiv u_\perp^2/2$ is a dummy integration variable. The decay rate of mode n goes like n^2, as is typical of diffusion problems. After a short time, the $n = 1$ term dominates. Retaining just this term, and evaluating $8/\pi^2 = 0.81$, we find

$$N_{\mathrm{tr}} \approx 0.81 I, \tag{A9}$$

$$I \equiv \int_0^\infty dx\, e^{-W}, \tag{A10}$$

$$W = x + Dt, \tag{A11}$$

$$D = \frac{(1+Z)2x(1+2ax)+2}{(1+2ax)^{5/2}}. \tag{A12}$$

To alleviate notation, we replaced $\hat{t}$ with t, $Z_{\rm eff}$ with Z, and defined $a \equiv u_p^{-2}$.

The upshot is an implicit integral equation for t:

$$I(t,a) = b \equiv \frac{N_{\rm tr}}{0.81}. \tag{A13}$$

Numerically finding t reveals it is linear in a for $a < 1$. We thus write $t = t_0 + at_1$ and expand for $a \ll 1$:

$$I \approx I(t_0,0) + at_1\partial_t I(t_0,0) + a\partial_a I(t_0,0) + O(a^2) = b. \tag{A14}$$

We choose t_0 such that $I(t_0,0) = b$. We find

$$I(t,0) = \int dx \exp[-W_0], \tag{A15}$$

$$W_0 = x + D_0 t, \tag{A16}$$

$$D_0 = 2(1+Z)x + 2. \tag{A17}$$

Performing the integral gives an implicit equation for t:

$$\frac{e^{-2t}}{1+2(1+Z)t} = b. \tag{A18}$$

This gives an exact formula for $N_{\rm tr}$ in the limit $u_p \to \infty$:

$$N_{\rm tr}(t) = \frac{0.81e^{-2t}}{1+2(1+Z)t} \qquad u_p \to \infty. \tag{A19}$$

The temporal decay of $N_{\rm tr}$ is thus not strictly exponential. This formula reflects the different mathematical character of parallel dynamics from electron-electron collisions $\to e^{-2t}$ and pitch-angle scattering from collisions with all species $\to (1+Z)t$. Eq. (A18) is transcendental, and can be "solved" in terms of the Lambert W function. We are interested in cases where $t < 1$, so we Taylor expand e^{-2t} to order t^2 and obtain

$$t_0 = \frac{1-b}{Y + [Y^2 - 2 + 2b]^{1/2}}, \qquad Y \equiv 1 + b(1+Z). \tag{A20}$$

This formula is valid (t_0 real) for b above $b_0(Z)$. For $Z = 0$ we have $b_0 = 5^{1/2} - 2 \approx 0.236$, and b_0 decreases with Z. For our choice of $N_{\rm tr} = 1/2$, $b = 0.617 > b_0$ for all Z. We have used the quadratic formula in a form that demonstrates the large-Z limit more clearly, which to leading order in Y is

$$t_0 \approx \frac{1-b}{2Y}, \qquad Y \gg 1. \tag{A21}$$

With $N_{\rm tr} = 1/2$ this becomes

$$t_0 \approx \frac{0.31}{2.62 + Z}. \tag{A22}$$

This form is accurate to within 10% for all $Z \geq 0$. The correction for finite a is

$$t_1 = -[\partial_a I/\partial_t I]|_{t=t_0,a=0} \tag{A23}$$

$$= -t_0 \frac{\int_0^\infty dx\ \exp[-W_0](\partial_a D)\ |_{a=0}}{\int_0^\infty dx\ \exp[-W_0] D_0}. \tag{A24}$$

The result is

$$t_1 = t_0 \frac{11 + 6Z + 10t_0(1+Z)}{(1+2t_0(1+Z))(2+Z+2t_0(1+Z))}. \tag{A25}$$

Using $N_{\rm tr} = 1/2$ and our approximate form for t_0,

$$t_1 \approx \frac{1.15 + 5.70Z^{-1} + 6.09Z^{-2}}{Z + 7.23 + 16.3Z^{-1} + 11.7Z^{-2}}. \tag{A26}$$

1. Validity of Fokker-Planck (FP) Model

Our FP model neglects large-angle scattering, which can detrap electrons in a single collision. We estimate their importance, and show that the FP detrapping rate dominates. As an example, we use the case from the end of Sec. VI, namely $n_e/n_{cr} = 0.1$, $T_e = 2$ keV, $\lambda_1 = 553$ nm, $k_2\lambda_{De} = 0.297$, $\omega_2/\omega_{pe} = 1.155$, and $Z_{\rm eff} = 4$, giving $\ln\Lambda_{ei} = 7.5$. Consider a trapped electron with $v_x = v_p$ and a typical $v_\perp = v_{Te}$, which is elastically scattered ($|\vec{v}| = (v_p^2 + v_{Te}^2)^{1/2} =$ const.) to the boundary of the trapping region in one collision. The electron's (initial, final) angle with respect to the $\hat{v}_x$ direction is (θ_I, θ_F):

$$\cos\theta_I = \frac{u_p}{\left(u_p^2 + 1\right)^{1/2}}, \tag{A27}$$

$$\cos\theta_F = \frac{u_p - u_{tr}/2}{\left(u_p^2 + 1\right)^{1/2}}. \tag{A28}$$

The critical angle $\theta_c = \theta_F - \theta_I$ separates large from small scattering angles, and is given without approximation by

$$2\delta N \cot^2\frac{\theta_c}{2} = -2\delta N + 2\frac{\omega}{\omega_{pe}}\delta N^{1/2} + (k\lambda_{De})^2 + k\lambda_{De}\left[(k\lambda_{De})^2 + 4(\omega/\omega_{pe})\delta N^{1/2} - 4\delta N\right]^{1/2} \tag{A29}$$

Figure 15 shows θ_c for our example parameters. For $\delta N \ll 1$, we have

$$\theta_c \approx \frac{2\delta N^{1/2}}{\left[(k\lambda_{De})^2 + 2(\omega/\omega_{pe})\delta N^{1/2}\right]^{1/2}}. \tag{A30}$$

We employ the potential for Yukawa-screened Coulomb scattering of an electron by an ion of charge Z: $V = -(U_e/r)e^{-r/\lambda_{De}}$ with $U_e \equiv Ze^2/4\pi\epsilon_0$. The quantum cross-section[56], in the first Born approximation, is

$$\frac{1}{\sigma_T}\frac{d\sigma}{d\Omega} = \frac{1+\delta}{4\pi}\frac{\delta}{(\delta + \sin^2(\theta/2))^2}. \tag{A31}$$

$\sigma_T \equiv 4\pi(1+\delta)^{-1}(U_e/\hbar\omega_{pe}u_p)^2$ is the total cross-section, and $\delta \equiv (\hbar\omega_{pe}/2u_pT_e)^2$ is unitless and typically small. For our example parameters, $\delta = 5.14 \times 10^{-9}$. The cross-section, integrated from θ_1 to θ_2, is

$$\frac{\sigma|_1^2}{\sigma_T} = (1+\delta)\delta\frac{\sin^2(\theta_2/2) - \sin^2(\theta_1/2)}{(\delta + \sin^2(\theta_1/2))(\delta + \sin^2(\theta_2/2))}. \tag{A32}$$

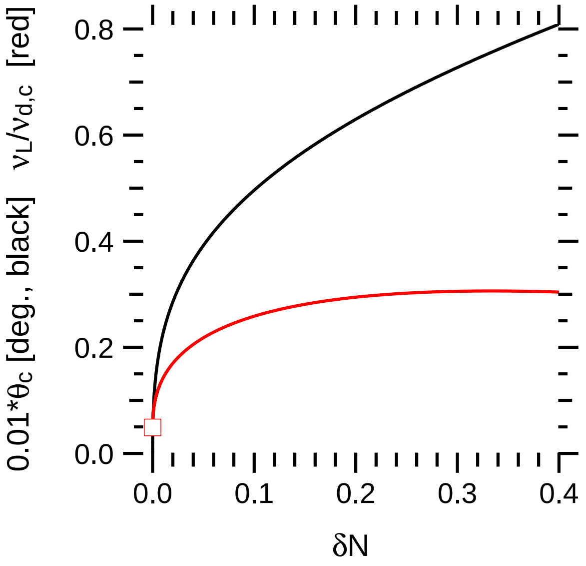

FIG. 15. (Color online.) Black: angle θ_c separating small- from large-angle scattering from Eq. (A29). Red: Ratio $\nu_L/\nu_{\mathrm{d,c}}$ from Eq. (A33), with the $\delta N = 0$ value marked.

The total cross section from $\theta_1 = 0$ to $\theta_2 = \pi$ is finite (without imposing any cutoffs) and equals σ_T. The cross sections for small-angle scattering σ_S ($\theta_1 = 0$ to $\theta_2 = \theta_c$) and large-angle scattering σ_L ($\theta_1 = \theta_c$ to $\theta_2 = \pi$) have the ratio $\sigma_L/\sigma_S = \delta(1+\delta)^{-1}\cot^2(\theta_c/2)$. For our example parameters $\sigma_L < 0.01\sigma_S$ for $\delta N > 5 \times 10^{-8}$. There are many more small- than large-angle scatters, which is necessary for a FP model to be valid.

The detrapping rate due to large-angle scatters is approximately the rate at which our typical electron undergoes one such scatter, i.e. $\nu_L = n_i \sigma_L v$. We compare ν_L for $1+\delta \approx 1$ to the FP detrapping rate, just due to electron-ion collisions and using $\hat{t} \approx \hat{t}_0$:

$$\frac{\nu_L}{\nu_{\mathrm{d,c}}} = \frac{0.36}{\ln \Lambda_{ei}} \frac{\delta N \cot^2(\theta_c/2)}{(k\lambda_{De})^2} \tag{A33}$$

$$\approx \frac{0.36}{\log \Lambda_{ei}} \qquad \delta N \ll 1. \tag{A34}$$

The ratio depends only on $\ln \Lambda_{ei}$ for small δN, so the FP result captures the basic parameter dependence. Large-angle scattering enhances the FP detrapping rate by a modest amount. For our parameters, $\nu_L/\nu_{\mathrm{d,c}} = 0.048$ at $\delta N = 0$, and the ratio is plotted in Fig. 15. Since the FP results were found for $\delta N \ll 1$, the comparison of ν_L and $\nu_{\mathrm{d,c}}$ may not be accurate at large δN.

[1] I. B. Bernstein, J. M. Greene, and M. D. Kruskal, Phys. Rev. **108**, 546 (1957).
[2] T. O'Neil, Phys. Fluids **8**, 2255 (1965).
[3] W. M. Manheimer and R. W. Flynn, Phys. Fluids **14**, 2393 (1971).
[4] G. J. Morales and T. M. O'Neil, Phys. Rev. Lett. **28**, 417 (1972).
[5] R. L. Dewar, Phys. Fluids **15**, 712 (1972).
[6] C. B. Wharton, J. H. Malmberg, and T. M. O'Neil, Phys. Fluids **11**, 1761 (1968).
[7] W. L. Kruer, J. M. Dawson, and R. N. Sudan, Phys. Rev. Lett. **23**, 838 (1969).
[8] T. Tajima and J. M. Dawson, Phys. Rev. Lett. **43**, 267 (1979).
[9] M. V. Goldman and D. F. DuBois, Phys. Fluids **8**, 1404 (1965).
[10] J. F. Drake, P. K. Kaw, Y. C. Lee, G. Schmidt, C. S. Liu, and M. N. Rosenbluth, Phys. Fluids **17**, 778 (1974).
[11] W. L. Kruer, *The Physics of Laser Plasma Interactions* (Westview Press, Boulder, CO, 2003).
[12] V. M. Malkin, G. Shvets, and N. J. Fisch, Phys. Rev. Lett. **82**, 4448 (1999).
[13] J. Lindl, P. Amendt, R. L. Berger, S. G. Glendinning, S. H. Glenzer, S. W. Haan, R. L. Kauffman, O. L. Landen, and L. J. Suter, Phys. Plasmas **11**, 339 (2004).
[14] S. Atzeni and J. Meyer-ter-Vehn, *The Physics of Inertial Fusion: Beam Plasma Interaction, Hydrodynamics, Hot Dense Matter* (Oxford University Press, Oxford, UK, 2004).
[15] E. I. Moses and C. R. Wuest, Fusion Sci. Tech. **47**, 314 (2005).
[16] N. B. Meezan, L. J. Atherton, D. A. Callahan, E. L. Dewald, S. Dixit, E. G. Dzenitis, M. J. Edwards, C. A. Haynam, D. E. Hinkel, O. S. Jones, O. Landen, R. A. London, P. A. Michel, J. D. Moody, J. L. Milovich, M. B. Schneider, C. A. Thomas, R. P. J. Town, A. L. Warrick, S. V. Weber, K. Widmann, S. H. Glenzer, L. J. Suter, B. J. MacGowan, J. L. Kline, G. A. Kyrala, and A. Nikroo, Phys. Plasmas **17**, 056304 (2010).
[17] H. X. Vu, D. F. DuBois, and B. Bezzerides, Phys. Rev. Lett. **86**, 4306 (2001).
[18] D. J. Strozzi, E. A. Williams, A. B. Langdon, and A. Bers, Phys. Plasmas **14**, 013104 (2007).
[19] D. Bénisti, D. J. Strozzi, L. Gremillet, and O. Morice, Phys. Rev. Lett. **103**, 155002 (2009).
[20] D. Bénisti, O. Morice, L. Gremillet, E. Siminos, and D. J. Strozzi, Phys. Rev. Lett. **105**, 015001 (2010).
[21] I. N. Ellis, D. J. Strozzi, B. J. Winjum, F. S. Tsung, T. Grismayer, W. B. Mori, J. E. Fahlen, and E. A. Williams, Phys. Plasmas (in press, DOI: 10.1063/1.4762853) (2012).
[22] S. Brunner and E. J. Valeo, Phys. Rev. Lett. **93**, 145003 (2004).
[23] L. Yin, B. J. Albright, H. A. Rose, K. J. Bowers, B. Bergen, D. S. Montgomery, J. L. Kline, and J. C. Fernández, Phys. Plasmas **16**, 113101 (2009).
[24] L. Yin, B. J. Albright, K. J. Bowers, W. Daughton, and H. A. Rose, Phys. Rev. Lett. **99**, 265004 (2007).
[25] J. E. Fahlen, B. J. Winjum, T. Grismayer, and W. B. Mori, Phys. Rev. E **83**, 045401 (2011).
[26] J. W. Banks, R. L. Berger, S. Brunner, B. I. Cohen, and J. A. F. Hittinger, Phys. Plasmas **18**, 052102 (2011).
[27] H. A. Rose and L. Yin, Phys. Plasmas **15**, 042311 (2008).
[28] N. A. Yampolsky and N. J. Fisch, Phys. Plasmas **16**, 072105 (2009).
[29] I. Y. Dodin and N. J. Fisch, Phys. Plasmas **19**, 012102 (2012).
[30] D. Bénisti, N. A. Yampolsky, and N. J. Fisch, Phys. Plasmas **19**, 013110 (2012).
[31] H. A. Rose, Bull. Am. Phys. Soc. **51** (2006), talk CO3.10, APS-DPP 2006, Philadelphia, USA.
[32] J. Banks and J. Hittinger, IEEE Trans. Plasma Sci. **38**, 2198 (2010).
[33] S. Skupsky, R. W. Short, T. Kessler, R. S. Craxton, S. Letzring, and J. M. Soures, J. Appl. Phys. **66**, 3456 (1989).
[34] P. L. Bhatnagar, E. P. Gross, and M. Krook, Phys. Rev. **94**, 511 (1954).
[35] B. D. Fried and S. D. Conte, *The Plasma Dispersion Function: The Hilbert Transform of the Gaussian* (Academic Press, New York, 1961).
[36] H. A. Rose and D. A. Russell, Phys. Plasmas **8**, 4784 (2001).
[37] D. J. Strozzi, A. B. Langdon, E. A. Williams, A. Bers, and S. Brunner, "Eulerian codes for the numerical solution of the kinetic equatioins of plasmas," (Nova Science Publishers, Inc., New York, 2011) Chap. 4.
[38] R. W. Short and A. Simon, Phys. Plasmas **5**, 4124 (1998).
[39] O. Skjæraasen, P. A. Robinson, and A. Melatos, Phys. Plasmas **6**, 3435 (1999).
[40] J. D. Huba, *NRL Plasma Formulary* (Naval Research Lab, Wash-

ington, DC, 2007).

[41] R. L. Berger, C. H. Still, E. A. Williams, and A. B. Langdon, Phys. Plasmas **5**, 4337 (1998).

[42] D. Strozzi, D. Hinkel, E. Williams, R. Town, P. Michel, L. Divol, R. Berger, and J. Moody, Bull. Am. Phys. Soc. **56** (2011).

[43] Y. Kato, K. Mima, N. Miyanaga, S. Arinaga, Y. Kitagawa, M. Nakatsuka, and C. Yamanaka, Phys. Rev. Lett. **53**, 1057 (1984).

[44] J. Garnier and L. Videau, Phys. Plasmas **8**, 4914 (2001).

[45] R. K. Kirkwood, P. Michel, R. London, J. D. Moody, E. Dewald, L. Yin, J. Kline, D. Hinkel, D. Callahan, N. Meezan, E. Williams, L. Divol, B. L. Albright, K. J. Bowers, E. Bond, H. Rose, Y. Ping, T. L. Wang, C. Joshi, W. Seka, N. J. Fisch, D. Turnbull, S. Suckewer, J. S. Wurtele, S. Glenzer, L. Suter, C. Haynam, O. Landen, and B. J. Macgowan, Phys. Plasmas **18**, 056311 (2011).

[46] N. A. Yampolsky and N. J. Fisch, Phys. Plasmas **18**, 056711 (2011).

[47] D. H. Froula, L. Divol, R. A. London, R. L. Berger, T. Döppner, N. B. Meezan, J. S. Ross, L. J. Suter, C. Sorce, and S. H. Glenzer, Phys. Rev. Lett. **103**, 045006 (2009).

[48] D. H. Froula, L. Divol, R. A. London, R. L. Berger, T. Döppner, N. B. Meezan, J. Ralph, J. S. Ross, L. J. Suter, and S. H. Glenzer, Phys. Plasmas **17**, 056302 (2010).

[49] D. H. Froula, private communication.

[50] T. Dewandre, J. R. Albritton, and E. A. Williams, Phys. Fluids **24**, 528 (1981).

[51] D. J. Strozzi, E. A. Williams, D. E. Hinkel, D. H. Froula, R. A. London, and D. A. Callahan, Phys. Plasmas **15**, 102703 (2008).

[52] R. K. Kirkwood, Y. Ping, S. C. Wilks, N. Meezan, P. Michel, E. Williams, D. Clark, L. Suter, O. Landen, N. J. Fisch, E. J. Valeo, V. Malkin, D. Turnbull, S. Suckewer, J. Wurtele, T. L. Wang, S. F. Martins, C. Joshi, L. Yin, B. J. Albright, H. A. Rose, and K. J. Bowers, J. Plasma Phys. **77**, 521 (2011).

[53] S. I. Braginskii, in *Reviews of Plasma Physics*, Vol. 1, edited by M. A. Leontovish (Consultants Bureau, New York, 1965) pp. 205–311.

[54] E. M. Epperlein and M. G. Haines, Phys. Fluids **29**, 1029 (1986).

[55] D. E. Hinkel, M. D. Rosen, E. A. Williams, A. B. Langdon, C. H. Still, D. A. Callahan, J. D. Moody, P. A. Michel, R. P. J. Town, R. A. London, and S. H. Langer, Phys. Plasmas **18**, 056312 (2011).

[56] D. J. Griffiths, *Introduction to Quantum Mechanics* (Prentice Hall, Upper Saddle River, NJ, 1995).